Thesis for the degree
Doctor of Philosophy

Submitted to the Scientific Council of the
Weizmann Institute of Science
Rehovot, Israel

עבודת גמר (תזה) לתואר
דוקטור לפילוסופיה

מוגשת למועצה המדעית של
מכון ויצמן למדע
רחובות, ישראל

By
Noam Matzliah

מאת
נעם מצליח

מדידת מעוות אופטו-מכני בענן אטומים קר
Observation of Optomechanical Strain in a Cold Atomic Cloud

Advisors: Prof. Nir Davidson
Prof. Roee Ozeri

מנחים: פרופ' ניר דודזון
פרופ' רועי עוזרי

May 2018

אייר תשע"ח

Table of contents

תקציר

אינטראקציות מושרות בין חלקיקים מהוות מרכיב בתיאוריות בפיסיקה מודרנית, כגון אלה של המודל הסטנדרטי ושל אינטראקציות בין-אלקטרוניות במוליכי-על. אטומים קרים מאפשרים לדמות בצורה פיזיקלית מערכות חלקיקים בעלי אינטראקציה, תוך מתן אפשרות לחקור אותן בדרכים שאינן נגישות במערכות המקוריות.

בעבודת גמר זו אני מדווח על תצפית של אינטראקציה מושרה מסוג חדש בין אטומים בענן אטומים קרים, שמאופיינת על ידי הדמיה של המעוות האופטו-מכני שהיא יוצרת. זו התצפית הישירה הראשונה של מעוות אופטו-מכני. המעוות מופעל על ענן אטומים תרמי או מנוון קוונטית, על ידי הארתו בקרן לייזר רבת עצמה, רחוקה מרזוננס אטומי והומוגנית. בתחום פרמטרים זה הענן מתנהג כעדשה שממקדת את קרן הלייזר. כתגובת נגד, על האטומים פועל כח הפוך בכיוונו לכיוון הטיית הקרן, שתלוי בפרופיל הצפיפות של הענן. אנו מדגימים ניסיונית תכונותיו החזויות הבסיסיות של כוח זה, ומבדילים אותו מן הכוחות המוכרים. המעוות שנצפה מגיע לרוויה, כך שבסופו של דבר מוגבל התנע שניתן להעביר לאטומים. כוח אופטו-מכני זה עשוי להיות יעיל בהשריית אינטראקציה בין-חלקיקית, הניתנת לשליטה אופטית.

Abstract

Inter-particle mediated interactions are part of modern physics theories, such as the Standard Model and electronic interactions within superconductors. Cold atoms enable to physically simulate interacting systems, while allowing for probing them in ways which are originally inaccessible.

In this thesis I report the observation of a new type of light-induced interactions between atoms in a cold atomic cloud, probed by imaging the resulting optomechanical strain. This is the first direct observation of strain in optomechanics. The strain is applied to thermal and quantum degenerate atomic clouds by an intense, far detuned homogeneous laser beam. In this regime the cloud acts as a lens which focuses the laser beam. As a backaction, the atoms experience a force opposite to the beam deflection, which depends on the density profile. We experimentally demonstrate the basic features of this force, distinguishing it from the well established forces. The observed strain saturates, ultimately limiting the momentum impulse that can be transferred to the atoms. This optomechanical force may effectively induce interparticle interactions, which can be optically tuned.

Acknowledgments

I would like to acknowledge the contributions of a number of people to the work described in this thesis. The first word of thanks must go to Nir and Roee, for being my personal professional teachers and scientific educators, and for providing me with the freedom and tools to concentrate on science.

I owe a great expression of gratitude to Asif Sinay, who introduced me with the lab he initiated its construction, taught me many of the skills needed for the demanding cold atoms research, and who served as a model for hard work and dedication.

Not much after me, Hagai Edri joined our lab. Most of my work in the lab was done with Hagai, including some hard time periods. The two of us performed the systems first published experiment, which I discuss in this thesis. Without Hagai's work I would have not reached this point.

I would also like to thank many of my colleagues and specifically Ziv Meir, Jonathan Coslovsky, Shamir Rosen, Gadi Afek, Gal Orenstein, David Eger, Slava Smartsev, Chene Tradonsky, Ronen Chriki, Vishwa Pal, Alok Kumar-sing, Gilad Barach, Arnaud Courvoisier, Oz Livneh, Boaz Raz, Alex Cheplev and Jonathan Friedman for numerous discussions, idea exchange, brainstorming, as well as arguing and taking coffee breaks.

I thank Rostyslav Baron for escorting and helping us all along with numerous construction projects - day and night. I thank Gershon Elazar, Guy Han and Yossi Shopen for their mechanical designing and manufacturing of many devices all over the scope of our research. Our private workshop is not less than a treasure to cherish. I thank our great electronics

expert, Yeruham Shimoni, designing with us and constructing tens of electronic devices needed in the experimental setup. I thank Yigal Shahar who helped us during the worst times, when we suffered vacuum breakdowns. Yigal is a national-class vacuum technological expert who taught us and equipped us with highly valuable knowledge. I thank Perla Zalcberg, Rachel Goldman and Hilla Shohat for dealing with the intensive management tasks essential for allowing me to dedicate myself solely to research. I thank Malka Paz for directing and escorting us while purchasing more than a million USD worth of scientific equipment used in our lab. I thank Yossi Drier for supporting our computers, which control the entire experimental setup. I thank Ezra Eliaho for helping us with tasks of various kinds. Ezra is one of the people who constitute our special departmental atmosphere.

Finally on a personal note I would like to thank my beloved wife, Tamar, for her support over all these years of endless work and harsh deadlines, raising together our four lovely boys. I thank my parents who taught me manners and respect, and believed in me all along.

The work on the machine will continue cooperatively by Hagai Edri and Boaz Raz. I wish them good luck and great success.

Chapter 1

Introduction

The achievement of Bose-Einstein condensation (BEC) [1–3] and of Fermi degeneracy [4–6], and the ability to tune interaction strengths by Feshbach resonances [7, 8] and to apply external potentials with optical lattices [9], opened the opportunity of probing many-body physics aspects using ultracold dilute gasses in a highly controlled manner. These advances enabled physics explorations in many research areas at the frontier, as well as state-of-the-art practical devices in the last twenty years. One research area considers a fundamental idea in modern high energy and condensed matter theory - inter-particle interactions induced by some mediator. All three forces included in the Standard Model (SM) of particle physics are mediated by bosonic carrier particles. Composite forces derived by renormalization of the SM, and effective forces in condensed matter theory are mediated by effective force carriers as well. The most famous such force is the phonon-mediated attraction between electrons in a superconductor.

There are two common forces lasers exert on atoms, which enter cold atoms experiments. These are termed the *scattering force* and the *dipole force* in the jargon of the cold atoms

research literature, and take the form [10]

$$\begin{aligned} \vec{f}_{dipole} &= -\frac{\hbar\Gamma^2}{8\Delta}\frac{\vec{\nabla}I}{I_s} \\ \vec{f}_{scattering} &= \frac{\hbar\Gamma^3}{8\Delta^2}\vec{k_L}\frac{I}{I_s}, \end{aligned} \tag{1.0.1}$$

where Δ is the lasers detuning from atomic resonance, , the width of the atomic transition, I, the laser beam intensity, I_s, the atomic saturation intensity, and $\vec{k_L}$, the laser wave number vector.

The scattering force originates from resonant absorption of photons by the atoms, which recoil in the direction of the photons wave number vector. This force is the cold atoms version of the *radiation pressure* in the optomechanics jargon. The scattering force is at the heart of key cooling mechanisms, such as magneto-optical traps and polarization gradient cooling schemes [11]. It accompanies any process of incoherent or coherent optical pumping [10]. In ultracold atoms experiments the scattering force is eventually avoided in order to prevent heating of the cloud, and sub-recoil cooling schemes are used, which do not involve resonant scattering [11]. The dipole force originates from coherent scattering of photons by the atoms from one occupied wave number vector to another [12]. This force appears only in the presence of a homogeneous laser beam, which as such, does not includes only a single wave number vector. This force is the cold atoms version of the *optical tweezing* force [13] in optomechanics jargon. The dipole force underlays optical traps [14] and optical lattices [15], used in almost all ultracold atoms experiments. Less commonly, the more exotic induced and non-induced dipole-dipole forces are used [16–19].

All mentioned forces act on single atoms. Collective forces can arise as higher order forces, such as entering light-assisted collisions due to multiple scattering. Such forces are collective in the sense they act only on atoms consisting an atomic cloud, and as such depend on the cloud density. As a result, collective forces can be viewed as forces (or interactions) induced between the atoms by the applied laser beam. Being higher order forces, collective forces scale with a higher power of the coupling between light and atoms. The forces I mentioned

originate from a single laser beam. More involved schemes, where a beam passes the atoms multiple times are used to create a large variety of higher order induced forces between atoms with many interesting outcomes [20–26]. Combinations of coherent laser beams are used to engineer artificial gauge fields [27] acting on single atoms. In addition, quantum degenerate atomic clouds can show unique forces associated with coherent processes within the clouds, such as superadiance [28].

My colleagues and I have constructed a machine for exploring many-body physics with ultracold gasses of ^{87}Rb (boson) and ^{40}K (fermion) atoms. Using our machine we managed to measure a new type of collective light-induced force between cold atoms in a thermal as well as quantum degenerate ^{87}Rb cloud, using a homogeneous single beam. This collective force, which we term *electrostriction*, surprisingly does not depend on the atomic cloud density and is first order in the light-atoms coupling. We used a far detuned high intensity laser beam to demonstrate the effect of the electrostriction force. We proved this is indeed a new force that differs from the well-known dipole and scattering forces and demonstrated its many-body character. In my thesis I present this experiment in detail and discuss future plans for further research on the topic, including inter-particle interactions within a BEC, pattern formation driven by modulational instability and self-trapping. In the near future our group plans to measure interactions between ^{87}Rb bosons mediated by bosonic excitation in a Fermi sea of ^{40}K fermions.

Our machine will serve as a generic research platform for many-body bosonic and fermionic physics. In particular we intend to focus on inducing mediated interactions between atoms and probe them in ways available for cold atoms research, while inaccessible in high energy or condensed matter setups.

In Chapter 2 I describe the theory we derived for the electrostriction force, the ways to probe it and its theoretical implications. These derivations are original. In Chapter 3 I survey our experimental setup and the main engineering considerations underlying its design. I cover our vacuum system, the atomic sources we use, and the series of trapping and cooling techniques used in order to get quantum degenerate ^{87}Rb and ^{40}K atomic clouds.

Chapter 4 is the heart of the thesis, describing the main findings of measuring the effect of the electrostriction force and its features. In Chapter 5 I summarize our findings and review two of our further research proposals for our system.

Chapter 2

Theory of Electrostriction in Cold Atomic Clouds

Light-matter interactions are at the core of cold atom physics. A laser beam illuminating atoms close to atomic resonance frequency will apply a scattering force on them, and an inhomogeneous laser beam far from resonance will mainly apply an optical dipole force [10]. An intense, far detuned homogeneous laser beam does not exert a significant force on a single atom, though when applied on inhomogeneous atomic clouds, it will. This was pointed out while studying lensing by cold atomic clouds in the context of nondestructive imaging [29].

The atom's electric polarizability makes atomic clouds behave as refractive media with an index locally dependent on the density. An atomic cloud thus behaves as a lens that can focus or defocus the laser beam. The atoms recoil in the opposite direction of the beam deflection due to momentum conservation. In solid lenses, this optomechanical force causes a small amount of stress with negligible strain, due to their rigidity. An atomic lens, however, deforms, making the force on the atoms observable by imaging their strain. We refer to this optomechanical force as electrostriction, since it resembles shape changes of materials under the application of a static electric field. Electrostriction can be viewed as an optically induced force between atoms, since the force each atom experiences depends on the local density of the other atoms.

Optomechanical forces are applied in experiments on refractive matter mainly by optical tweezers [30], using structured light. Less commonly, such forces can be applied by homogeneous light using angular momentum conversion due to the material birefringence [31], or using structured refractive material shapes [32]. Optomechanical forces implemented by such techniques are used for optically translating and rotating small objects (e.g. in [33]). By applying electrostriction on cold atoms we gain access to the effect of optical strain - an aspect in optomechanics not directly studied yet in spite of its importance in current research [34].

Interactions between cold atoms can appear naturally or be externally induced and tuned. Tuning is mostly done using a magnetic Feshbach resonance, which was used to demonstrate many important physical effects such as BEC collapse and explosion [35], Feshbach molecules [36, 37], BEC-BCS crossover in strongly interacting degenerate fermions [38–40], and Fermi superfluidity [41–44]. Interactions are also tuned by optical Feshbach resonance [45], optical cavities [20], or radio frequency Feshbach resonance [46]. Interactions can be induced by shining a laser beam on the atoms and creating a feedback mechanism to their response by an externally pumped cavity or a half cavity [21–26]. The electrostriction force reported here is a new kind of induced force between atoms, and may be useful in cold atoms and quantum degenerate atom experiments.

In this chapter I derive the theory for the electrostriction force under research in this work, its effect on time of flight measurements, and some of its theoretical implications regarding self trapping, effective interaction tuning and pattern formation.

2.1 The electrostriction force

A plane wave propagating in the $\hat{z}$ direction has a time-dependent phase of $(k_L z - \omega_L t)$. k_L denotes the wave number of the incident light, and ω_L - its angular frequency.

After passing through an infinitesimal section of width dz in an atomic cloud, the light will acquire a phase of $\phi = k_L n_{ref} dz$, where the local refractive index of the cloud is given by

$n_{ref}(\vec{r}) = 1 + \Re e(\tilde{\chi})/2$. Here $\tilde{\chi}$ is the Fourier transform of the atomic electric susceptibility. An expression for $\tilde{\chi}$ is derived by solving the optical Bloch equations for two-level atoms [47]

$$\tilde{\chi} = i\frac{3}{8\pi^2}n\lambda^3(\rho_{11}-\rho_{22})\frac{\Gamma}{\frac{\Gamma}{2}-i\Delta}. \tag{2.1.1}$$

Here n is the atomic cloud density, λ, the light wavelength, ρ_{11} and ρ_{22}, the populations (the diagonal elements of the density matrix ρ) of the two atomic states denoted $|1\rangle$ and $|2\rangle$, Γ is the width of the atomic transition, and Δ, the detuning of the light.

In our experiment we use a far detuned laser $|\Delta| \gg \Gamma$ and to a good approximation the atoms stay in the ground state so that $\rho_{11} \approx 1$ and $\rho_{22} \approx 0$. Under these conditions I can approximate the phase ϕ by

$$\phi \approx k_L dz - \frac{\sigma_0}{4}\frac{\Gamma}{\Delta}ndz. \tag{2.1.2}$$

$\sigma_0 = 3\lambda^2/(2\pi)$ being the cross section for photon scattering from an atom. After passing the infinitesimal section at point (x_0, y_0, z_0), the light will have a phase of $\phi(x,y,z_0)+k_L z-\omega_L t$ at point (x,y,z). The corresponding Poynting vector under the eikonal approximation [48] takes the form $\vec{S} \approx \omega_L^{-1}|\vec{E}|^2\vec{\nabla}[\phi(x,y,z_0)+k_L z]/(2\mu_0) = \omega_L^{-1}|\vec{E}|^2(k_L\hat{z}+\vec{\nabla}_{x,y}\phi)/(2\mu_0)$, where μ_0 is the vacuum permeability and $\vec{E}$ is the electric field amplitude associated with the light. The Poynting vector is the electromagnetic energy E_γ flux. Using the dispersion relation of light $E_\gamma = cP_\gamma$, the electromagnetic momentum $\vec{P}_\gamma$ flux is $\vec{S}/c$. By momentum conservation, the momentum change per unit time in an infinitesimal section is $d\vec{P}_a/dt = dA_\perp\vec{S}/c$, where the integration is over surface elements $dA_\perp = d\vec{A}\cdot\hat{S}$ surrounding the section. This momentum change corresponds to the total force on the atoms in the section $\vec{f}_{total} = d\vec{P}_a/dt$. Dealing with clouds which cause only slight changes in the Poynting vector, its direction will stay approximately the same, and thus $\frac{1}{c}dA_\perp\vec{S} \approx \frac{1}{c}\Delta\vec{S}dA$, where $\Delta\vec{S}$ is the difference in the Poynting vector after and before passing the infinitesimal section, and dA is the area of incidence of the section. Plugging the speed of light $c = \frac{1}{\sqrt{\varepsilon_0\mu_0}}$, the electric field intensity $I = c\varepsilon_0|\vec{E}|^2/2$ and the vacuum permittivity ε_0, I get

$$\vec{f}_{total} = -\frac{k}{2\mu_0\omega_L^2}|\vec{E}|^2\vec{\nabla}_{x,y}\phi dA = \frac{\sigma_0}{4}\frac{\Gamma}{\Delta}\frac{I}{\omega}\vec{\nabla}_{x,y}ndzdA. \tag{2.1.3}$$

The total force is equally distributed among $dN = ndzdA$ atoms consisting the infinitesimal section, and thus each atom feels a force of

$$\vec{f}_{es} = \frac{\vec{f}_{total}}{dN} = \frac{\sigma_0}{4}\frac{\Gamma}{\Delta}\frac{I}{\omega_L}\frac{\vec{\nabla}_{x,y}n}{n} = \frac{\hbar\Gamma^2}{8\Delta}\frac{I}{I_s}\frac{\vec{\nabla}_{\perp}n}{n}, \tag{2.1.4}$$

where I used the relation between the scattering cross section and the saturation intensity $\sigma_0 = \hbar\omega_L\Gamma/(2I_s)$.

I note that the cloud imprints a phase on the laser light passing through it, and this phase does not translate to intensity gradients by means of free propagation in the cloud itself (thin lens approximation). This is in contrast to cavity mediated interaction schemes described in [49], and to half-cavity schemes as in [25, 26]. In these works, the round trip in the cavity translates laser phase changes into intensity changes felt by the atoms.

The derivation I presented does not capture the microscopic origin of the electrostriction force. It seems to us that attempts to understand the microscopics underlying electrostriction must give rise to a force, which is at least second order in the light-atoms coupling, while our macroscopic argument provides a first order expression. No electrostriction force will act on a single atom. This indicates that electrostriction force acting on a probe atom stems from its response to the original laser beam combined with the radiation from all neighboring atoms. Increasing the light-atoms coupling by a factor of α, will increase the radiation from the neighboring atoms by α, and increase the response of the probe atom to a given field by α. We thus deduce the probe atom will feel a force, which scale as α^2, so that electrostriction seems to be second order in the light-atoms coupling. Currently we do not have a microscopic picture of electrostriction. Such a picture might shed light on our observation of electrostriction saturation, and on the mesoscopic limit, where the atomic cloud is too dilute to be treated as a refractive media of a spacially smooth refractive index.

2.2 Electrostriction and time of flight measurements

For a nondegenerate cloud with temperature T, the phase space distribution of the atomic cloud in a harmonic trap is $f_0(\vec{r},\vec{p}) \approx f_0 e^{\beta(\mu-H)}$. Here $H = p^2/(2m) + U(\vec{r})$ is the single particle Hamiltonian, $U = m/2\sum_{i=1}^{3}\omega_i^2 x_i^2$, the trapping potential, $\beta = 1/(k_B T)$, m, the atomic mass, $\vec{r}$ and $\vec{p}$ are position and momentum, ω_i, the harmonic trap angular frequencies, and f_0, a normalization constant setting the integral $1/h^3 \int d^3p d^3r f_0(\vec{r},\vec{p}) = N$ to the total number of atoms in the cloud N. The spacial density distribution of the cloud in the trap is $n_0(\vec{r}) = 1/h^3 \int d^3p f_0(\vec{r},\vec{p}) = f_0/(\lambda_{th}^3) e^{\beta(\mu-H)}$, where $\lambda_{th} = \sqrt{2\pi\hbar^2/(mk_B T)}$ is the De-Broglie thermal wavelength of the atoms. An electrostriction beam will apply to the cloud a force (2.1.4) of the form

$$\vec{f}_{es} = m\beta \frac{\hbar\Gamma^2}{4\Delta}\frac{I}{I_s}\sum_{i=x,y,z}\omega_i^2 x_i \hat{x}_i. \tag{2.2.1}$$

After shining the laser beam along $\hat{z}$ for a short time $\tau_p \ll \omega_i^{-1}$, the phase space distribution of the atoms will be $f_1(\vec{r},\vec{p}) = f_0\left[\vec{r},\vec{p} - \tau_p \vec{f}_{es}(\vec{r})\right]$. If the cloud is released from its trap right after the laser pulse and expends ballistically, its density distribution will be:

$$\begin{aligned} n_{TOF}(\vec{r},t,\tau_p) &= \frac{1}{h^3}\int d^3p f_1\left(\vec{r} - \frac{\vec{p}}{m}t, \vec{p}\right) = \left(\prod_{i=x,y,z} b_i\right)^{-1} n_o\left(\frac{x}{b_x}, \frac{y}{b_y}, \frac{z}{b_z}\right) \\ b_{x,y}(t,\tau_p) &= \sqrt{\left(1 - \tau_p\beta\frac{\hbar\Gamma^2}{8\Delta}\frac{I}{I_s}\omega_{x,y}^2 t\right)^2 + \omega_{x,y}^2 t^2} \\ b_z(t) &= \sqrt{1+\omega_z^2 t^2}. \end{aligned} \tag{2.2.2}$$

b_i are the expansion factors of the cloud during ballistic expansion along $\hat{x}_i$. The sizes of the cloud during time of flight are thus given by

$$\begin{aligned} \sigma_{x,y} &= \sqrt{\frac{k_B T}{m\omega_{x,y}^2}}\sqrt{\left(1 - \frac{\hbar\Gamma}{k_B T}\frac{\Gamma}{8\Delta}\frac{I}{I_s}\omega_{x,y}^2 t\,\tau_p\right)^2 + \omega_{x,y}^2 t^2} \\ \sigma_z &= \sqrt{\frac{k_B T}{m\omega_z^2}}\sqrt{1+\omega_z^2 t^2}. \end{aligned} \tag{2.2.3}$$

The above derivation relies on the impulse approximation. In order to check its validity, we numerically solved the dynamics of the atomic cloud when applying electrostriction on it using a phase space simulation. The simulation results coincide with our analytic predictions for all measurements presented here, confirming the impulse approximation. An example is given in Fig. 4.4. It turns-out that electrostriction saturates before the impulse approximation breaks, so we could not compare data to simulation results in this interesting regime which we cannot treat analytically. Further theoretical considerations regarding the above derivation are detailed in Appendices C.1 and C.3.

2.3 Self trapping

With a blue detuning, the strain laser can be adjusted to cause a thermal atomic cloud to be self-trapped by its own strain. A thermal cloud trapped in some external potential $U_{\text{ext}}(\vec{r})$ will have a Maxwell-Boltzmann spacial density $n(\vec{r}) \propto e^{-\beta U_{\text{ext}}}$. Under the effect of an electrostriction laser it will experience a force [Eq. (2.1.4)]

$$\vec{f}_{\text{es}} \propto \frac{\vec{\nabla}_{\perp} n}{n} \propto \vec{\nabla}_{\perp} U_{\text{ext}} \tag{2.3.1}$$

proportional to the force applied by $U_{ext}(\vec{r})$ in the directions transverse to the electrostriction laser beam. By turning off the external potential and rapidly turning on a blue detuned laser one can demonstrate self-trapping of the cloud in the transverse directions. This will be achieved choosing a working point at which the relation

$$\frac{\hbar\Gamma}{k_B T} \frac{\Gamma}{8\Delta} \frac{I}{I_{\text{s}}} = 1 \tag{2.3.2}$$

holds. This relation can be fulfilled, with a laser of power $P = 220$ mW and detuning 2 THz, suffering a spontaneous photon scattering rate of only 0.3 Hz. Notice this exotic effect is predicted to work for external potentials of any shape or origin. A more involved scheme using two laser beams can be applied to get self-trapping in all three dimensions.

In steady state such considerations would imply the electrostriction force, which optical dipole trap beams exert on the trapped atoms, is comparable to the trapping force itself. If this was true, the breathing and dipole modes of noninteracting thermal atoms in a dipole trap should deviate considerably from two. We were not able to observe such a deviation, probably due to the saturation we measured at long times and since Eq. (2.1.4) ignores light momentum redistribution associated with the trapping mechanism itself. The validity of (2.3.1) and (2.3.2) for steady state and for inhomogeneous beams is questionable.

2.4 Effective interaction tuning

An electrostriction laser beam applied to a two-dimensional BEC with a homogeneous density $|\psi(\vec{r})|^2 = n(\vec{r}) = n_0$ will exert a potential [Eq. (4.1.1)] which can be expanded as,

$$U_{\rm es} \approx -\frac{\hbar\Gamma^2}{8\Delta}\frac{I}{I_{\rm s}}\frac{n(\vec{r})-n_0}{n_0} \tag{2.4.1}$$

for small deformations of the spacial BEC density profile. Plugging Eq.(2.4.1) in the Gross-Pitaevski equation governing the BEC dynamics I get:

$$\begin{aligned} i\hbar\frac{\partial\psi}{\partial t} &= \left(-\frac{\hbar^2}{2m}\nabla^2 + g|\psi|^2 + U_{\rm es}\right)\psi \\ &\approx \left(-\frac{\hbar^2}{2m}\nabla^2 + \tilde{g}|\psi|^2 + const\right)\psi \\ \tilde{g} &= g - \frac{\hbar\Gamma^2}{8\Delta}\frac{I}{I_{\rm s}}\frac{1}{n_0}. \end{aligned} \tag{2.4.2}$$

The electrostriction laser effectively modifies the interparticle interaction strength g at the mean-field level, mimicking the effect of a Feshbach resonance, without really changing the scattering length. The interaction can be made repulsive (attractive) using a red (blue) detuned laser. A laser of power $P = 4$ W and detuning 4 THz can effectively modify the scattering length of ^{87}Rb to be about 60 times larger, suffering a spontaneous photon scattering rate of only 1.4 Hz. One can extend the scheme we suggest to a three-dimensional BEC using two

perpendicular electrostriction beams, avoiding interference by means of a frequency shift and perpendicular polarizations.

2.5 Pattern formation

A BEC with attractive effective interactions induced by an electrostriction laser will be unstable to spacial density modulations, seeded by some noise in the cloud density profile. The pattern formation process within a BEC can be derived using the Gross-Pitaevski equation [Eq. (2.4.2)], which is identical in form to the wave equation describing light propagation in an optical fiber with a Kerr nonlinearity [50]. I can thus rewrite the result in this reference for our case obtaining the dispersion relation $\omega(k)$ for disturbances of the BEC over its unstable stationary state

$$\omega^2 = \left(\frac{\hbar k^2}{2m}\right)^2 \left(1 + \frac{2n_0\tilde{g}}{\frac{\hbar k^2}{2m}}\right), \tag{2.5.1}$$

where $\tilde{g}$ was defined in Eq. (2.4.2). One can see that when the electrostriction-induced effective attraction overcomes the repulsive background interaction ($\tilde{g} < 0$), the angular frequency ω becomes imaginary for $0 < k < k_c$, where

$$\frac{\hbar k_c^2}{2m} = -2n_0\tilde{g}. \tag{2.5.2}$$

In this regime, the angular frequency gets a maximal amplitude value at $k = k_p$, where $k_p^2 = k_c^2/2$.

A modulation having a wave number k_p stemming from a BEC density fluctuation or an electrostriction beam intensity fluctuation, will grow exponentially faster than in any other wave number. The BEC density profile will thus get increasingly modulated at wave number k_p and will reach a point, where the small deformation approximation used in deriving Eq. (2.4.2) breaks down. We expect an eventual stabilization of the process, since the natural repulsion of ^{87}Rb atoms, which is linear in the density, will overcome the electrostriction

potential, which is logarithmic in the density. This analysis is similar to the one in [51] in the context of cold atoms.

2.6 In-situ density shape change

Since electrostriction can be viewed as effectively inducing interparticle interactions, we suggest measuring the effect of this interaction in steady state. We predict that application of an electrostriction laser beam on a trapped cloud will change its shape along the transverse directions.

An interacting zero-temperature BEC consisting of N atoms of mass m trapped in a harmonic trap of angular frequencies ω_i along the $\hat{x}_i$ axis will have a density of [52]

$$\begin{aligned} n &= \frac{15}{8\pi}\frac{N}{\prod_i x_{i,c,0}}\max\left(1-\sum_{i=1}^{3}\frac{x_i^2}{x_{i,c,0}^2},0\right) \\ x_{i,c,0} &= \sqrt{\frac{2\mu}{m\omega_i^2}} \\ \mu^{\frac{5}{2}} &= \frac{15\hbar^2\sqrt{m}}{2^{\frac{5}{2}}}N\omega_1\omega_2\omega_3 a. \end{aligned} \tag{2.6.1}$$

μ denotes the condensate chemical potential, and a is the interparticle collisional scattering length. The corresponding electrostriction potential experienced by the BEC will be [Eq. (4.1.1)]

$$U_{es} = -\frac{\hbar\Gamma^2}{4\Delta}\frac{I}{I_s}\ln\left[\max\left(1-\sum_{i=1}^{3}\frac{x_i^2}{x_{i,c,0}^2},0\right)\right]. \tag{2.6.2}$$

Expanding the joint potentials (trap and electrostriction) around the trap origin I find shifted trap angular frequencies given by

$$\tilde{\omega}_i^2 = \omega_i^2 + \frac{\hbar\Gamma^2}{4\Delta}\frac{I}{I_s}\frac{2}{m\tilde{x}_{i,c,0}^2}, \tag{2.6.3}$$

where the BEC size and chemical potential will self-consistently change to:

$$\begin{aligned} \tilde{x}_{i,c,0} &= \sqrt{\frac{2\tilde{\mu}}{m\tilde{\omega}_i^2}} \\ \tilde{\mu}^{\frac{5}{2}} &= \frac{15\hbar^2\sqrt{m}}{2^{\frac{5}{2}}} N_0 \tilde{\omega}_1 \tilde{\omega}_2 \omega_3 a. \end{aligned} \tag{2.6.4}$$

Solving for $\tilde{\omega}_i$, $\tilde{x}_{i,c,0}$ and $\tilde{\mu}$ can be done numerically. I rewrite Eq. (2.6.3) as

$$\left(\frac{\tilde{\omega}_i}{\omega_i}\right)^2 = 1 + \frac{2U_{AC}}{\tilde{\mu}}, \tag{2.6.5}$$

where $U_{AC} = -\frac{\hbar\Gamma^2}{8\Delta}\frac{I}{I_s}$ is the AC Stark shift of the atoms due to the electrostriction laser beam. This expression provides a simple way to estimate the strength of the electrostriction effect on the shape of the condensate. Note the changes appear only along the directions perpendicular the the beam propagation. A BEC with a chemical potential of a 2 kHz $\times \hbar$ shined by a laser of intensity 85 mW/ cm^2 and detuning 100 GHz, will feel a trap with $\left(\frac{\tilde{\omega}_i}{\omega_i}\right)^2 \approx 1.5$, which should be measurable. The scattering probability will be limited to 1% during five oscillation periods in a trap with $\omega_x = 2\pi \times 45$ Hz. The low intensity is needed to avoid considerable scattering during the electrostriction laser intensity ramp. The intensity ramp should be performed during a few oscillation periods in order to keep the process adiabatic, not heating the BEC.

An analogous derivation shows a thermal cloud of temperature T will feel a trapping frequency shift according to

$$\left(\frac{\tilde{\omega}_i}{\omega_i}\right)^2 = 1 + \frac{2U_{AC}}{k_B T}. \tag{2.6.6}$$

I note that the trapping frequency shift can be detected by in-situ density shape changes and by breathing modes of shifted frequency. The dipole oscillation mode (center of mass oscillations) will not be affected though. A measurement of a frequency inconsistent with the dipole oscillation mode frequency will provide conclusive evidence for attributing induced interactions to electrostriction. This is analogous to the BEC breathing mode having a frequency deviating from twice the trap frequency [53].

We did not measure a frequency shift when the electrostriction laser beam was on. We suspect that for some reason electrostriction works only during a transient time period. This is consistent with the observed and unexpected saturation of the electrostriction force [see Chapter 4], in particular as a function of time. In this context I note that also inhomogeneous laser beams, such as used in optical traps, should exert electrostriction force as well. No corresponding frequency shift is observed in dipole traps. I note though that one cannot use Eq. (2.1.4) for the electrostriction force of trapping beams, since the effect on the trapping beams themselves need to be taken into account when writing the momentum conservation condition used in the derivation in Section 2.1.

Chapter 3

Experimental Setup

The experimental setup was originally designed by Asif Sinay as a platform for exploring quantum degenerate gases. Asif laid the foundation for the construction of the system, while all three of us completed its construction. Since then, Hagai and I made major changes in the setup. For completeness I will describe the system as a whole.

In our system, all experiments include a series of steps aimed at getting enough atoms with a large enough phase space density and enough lifetime. The atoms are initially cooled in a double species 2D magneto-optical trap (MOT), which feeds a 3D MOT in a nearby chamber. The 3D MOT is loaded until it collects enough atoms. The atomic clouds in the MOT are compressed in a stage termed compressed MOT (CMOT) to get high density clouds. Then polarization gradient cooling (PGC) is performed aimed at cooling the clouds as much as possible. The cold and dense atoms are then optically pumped (OP) to a state of highest high-field seekers and are loaded to a magnetic trap (MT). The trap is moved to a ultra-high vacuum (UHV) chamber, the *science chamber*, by means of a magnetic transport. In the science chamber the atoms are loaded to a quadrupole Ioffe magnetic trap (QUIC), in which the ^{87}Rb atoms are evaporated by a long RF sweep, sympathetically cooling the ^{40}K atoms. The atoms are eventually loaded to a far-off resonance crossed dipole trap (FORT). ^{87}Rb (^{40}K) atoms are pumped to their lowest Zeeman state by a MW (RF) sweep. The mixture is further evaporated to quantum degeneracy. In the following sections I detail each of these

preparation steps. Manipulating and probing the atoms is mainly done using lasers, and thus I summarize all laser preparations in Appendix B for convenience. We use fluorescence imaging for measurements in the MOT chambers and absorption imaging for the science chamber.

3.1 Vacuum system

Ultracold atom experiments require UHV in order to isolate the atoms from colliding with background particles, obtaining sufficient coherence time and lifetime. For this purpose, our setup consists of a set of connected vacuum chambers. It includes a Pyrex chamber (2D MOT), a stainless steel (316L SS) chamber (3D MOT), a stainless steel tube for differential pumping, and a Pyrex chamber (science cell). The vacuum system is presented in Fig. 3.1.

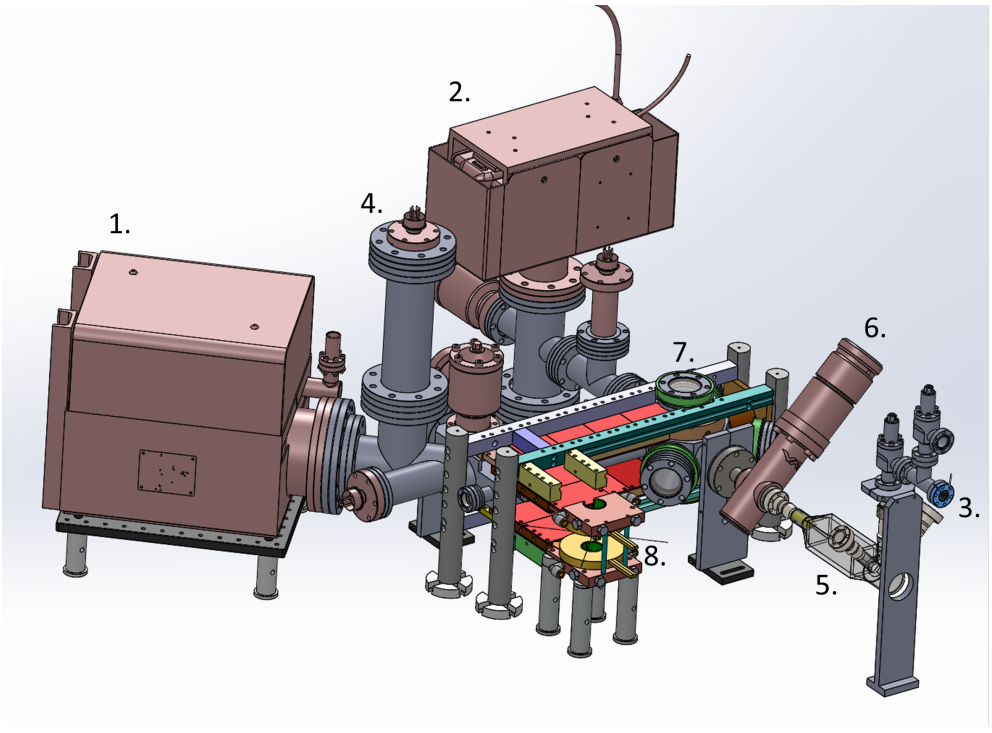

Figure 3.1: Schematic view of the vacuum system and the magnetic field coils. 1. Ion pump, $150\frac{\mathrm{L}}{\mathrm{sec}}$. 2. Ion pump, $55\frac{\mathrm{L}}{\mathrm{sec}}$. 3. CapaciTorr Pump. 4. Titanium sublimation pump. 5. 2D MOT chamber. 6. Gate valve. 7. 3D MOT chamber (covered with transport coils). 8. Science cell (covered by tow of the QUIC coils).

The 2D MOT chamber is pumped by a $0.5\frac{\mathrm{L}}{\mathrm{sec}}$ pump (CapaciTorr CF16 MK2, SAES), the 3D MOT chamber by a $55\frac{\mathrm{L}}{\mathrm{sec}}$ ion pump (VacIon plus starCell, Varian), and the Science chamber by a $150\frac{\mathrm{L}}{\mathrm{sec}}$ ion pump (VacIon plus starCell, Varian) and a Titanium sublimation pump (TSP filament cartridge source 9160050, Varian) internally coated by a Non-Evaporative Getter coating (GSI). This way the pressure in the 2D MOT chamber is kept at a few 10^{-8} Torr, in the 3D MOT chamber - a few 10^{-10} Torr and in the science chamber - about 10^{-11} Torr. These values change over time and through dispenser operation and are estimated by the ion pumps readouts, vacuum gauges installed in the system, and the lifetime of the atoms trapped in the chambers.

3.2 Atomic source - 2D magneto-optical trap

As a starting point for the atoms in our system we constructed a ^{87}Rb and ^{40}K 2D MOT, fed by dispensers. We chose a 2D MOT for the following advantages:

- Dispensers replacement would not require vacuum chamber exposure to atmospheric pressure, since it can be performed after closing a gate valve (48124-CE01, VAT) separating the 2D and 3D MOT chambers. This saves considerable time and effort, since there is no need to dis-assemble the optics surrounding the vacuum system and re-bake it. Baking of the 2D MOT chamber is unnecessary, since there is no need for pressures lower than 10^{-8} Torr in it.
- The pressure in the 3D MOT chamber can be kept low, since it is isolated from the dispensers by a differential pumping element we designed. This increases the lifetime of atoms in the 3D MOT, which may eventually allow transferring more atoms to the science cell.

Based on a design by the group of Yoav Sagi in the Technion, we designed an all-Pyrex uncoated 2D MOT chamber made by precision glassblowing LTD. The chamber includes:

- Four optical rectangular window parts of size 40X100cm for the main 2D MOT beams.
- A rear circular optical window of diameter 38 mm for a push beam.
- A front $1.33''$ flange for connection with the 3D MOT.
- Two rear legs with $1.33''$ flanges for dispenser feedthroughs.
- One rear leg with $1.33''$ flange on a bellow for pumping.

We avoided metallic parts in the chamber, to reduce sticking of ^{40}K to the chamber walls. For the 2D MOT we use two retro-reflected main beams and a retro-reflected push beam.

In order of maintaining a pressure difference between the 2D and 3D MOT chambers we designed a differential pumping tube of conical drill within, according to the following considerations:

- Our goal is to maintain a pressure of 10^{-11} Torr in the 3D MOT chamber and of 10^{-8} Torr in the 2D MOT chamber without the dispensers turned on.
- The conical drill should allow an atomic beam which spreads by an angle of at least 50 mrad – larger than atomic beam spreads reported by other research groups [54].
- The smaller hole in the tube should have a diameter of at least 2 mm allowing easy alignment of the cooled atomic beam and being similar to systems of other research groups.
- The end of the tube should be of polished elliptical cross-section cut 45° from the tube axis, so it would be used as a mirror for the push beam. This determines the tube length.

We decided not to use a mirror attached to the differential pumping tube's end, since such a mirror was reported to chemically react with ^{40}K atoms, severely reducing the mirror reflectance.

Under the above considerations we designed a differential pumping tube of length 11.5 cm, diameter of 11 mm, and conic hole with sizes of 2 mm and 9 mm at its edges. It provides a differential pumping pressure ratio of 10^{-3}, consistent with performance of similar systems. It turned-out that in order to get enough ^{40}K atoms we need to operate the dispensers at currents that increase the 2D MOT chamber pressure to a level that perturbs the system. We thus directly pump the 2D MOT chamber.

We produced the magnetic field needed for the 2D MOT operation by two perpendicular coil pairs each in an anti-Helmholtz configuration. Each coil pair was measured to produce a magnetic field gradient of $6.2\frac{\text{Gauss}}{\text{cm A}}$.

Figure 3.2: Side view of our ^{87}Rb 2D MOT by an IR camera. The shiny elongated glow on the left part is the 2D MOT fluorescence. On the right side the tip of the differential pumping tube with its 2 mm hole is shown.

We use four Rb and four K dispensers installed to the 2D MOT chamber at two of its legs. We installed the two species on separated legs to reduce coating of one dispenser type with atoms of the other type. The Rb dispensers (AS-Rb87-25-C, alvatec) containing 25 mg of metallic Rb enriched with ^{87}Rb to the level of 98%. We use two K dispensers (AS-KCl-Ca-2,5-3F, AlfaVakuo) containing 2.5 mg KCl salt enriched with ^{40}K to a level of 10%, mixed with 5.38 mg of Ca, and two dispensers with twice as much of these constituents. The enriched K dispensers were produced by AlfaVakuo according to [55] using enriched KCl salt from Trace Sciences International Inc.

We activated the dispensers while pumping the 2D MOT chamber with a turbo pump. We observed ^{87}Rb fluorescence by passing a beam along the chamber scanning its frequency around resonance. We then turned on the magnetic field and observed a small 2D MOT imaging from the rear of the chamber (without using the push beam yet). A good cross check was observing no 2D MOT when the 2D MOT coils run current in the opposite direction. The 2D MOT fluorescence signal is maximized by adjusting all available parameters. It is aligned to the conic drill in the differential pumping tube by biasing one coil of each coil pair using a manually variable resistor in parallel. The push beam is added and a clear ^{87}Rb 2D MOT (see Fig. 3.2) can be seen through an IR viewer. The 2D MOT is then optimized together with the 3D MOT to maximize atom loading. The ^{40}K 2D MOT cannot be seen

directly in the 2D MOT chamber, and is optimized by the 3D MOT. We use laser beams of powers summarized in Table 3.1. The 2D MOT laser beams are $2''$ in diameter. We operate the 2D MOT coils at 2.4 A.

Table 3.1: MOT laser beam total powers used in our setup.

^{87}Rb	3D MOT	Cooler	190 mW
		Repump	26 mW
	2D MOT	Cooler	140 mW
		Repump	10 mW
^{40}K	3D MOT	Cooler	170 mW
		Repump	90 mW
	2D MOT	Cooler	160 mW
		Repump	30 mW

The push beam carries about 10% of the 2D MOT cooler power. The MOT laser beam detunings are summarized in Table 3.2 (^{87}Rb repump is always resonant).

Table 3.2: MOT laser beam detunings. The ^{87}Rb cooler is detuned from the $F = 2 \rightarrow F' = 3$ transition. The ^{87}Rb repump is detuned from the $F = 1 \rightarrow F' = 2$ transition. The ^{40}K cooler is detuned from the $F = 9/2 \rightarrow F' = 11/2$ transition. The ^{40}K repump is detuned from the $F = 7/2 \rightarrow F' = 9/2$ transition.

Laser		Detuning	
^{87}Rb	Cooler	-11.8 MHz	-1.94Γ
^{40}K	Cooler	-22.2 MHz	-3.7Γ
	Repump	-23.4 MHz	-3.9Γ

The 2D MOT allows loading of more than 10^9 ^{87}Rb atoms and a few 10^8 ^{40}K atoms with a long lifetime of 10 sec in the 3D MOT chamber, as measured in a magnetic trap. Compared to operating the same system with dispensers in the 3D MOT chamber feeding it directly, the 2D MOT increased the number of ^{40}K atoms in the 3D MOT by a factor of five, the loading time increased from 1.5 sec to 7 sec, the pressure in the 3D MOT chamber decreased from 3×10^{-9} Torr to a few 10^{-10} Torr, and the 3D MOT lifetime increased from 2 sec to 10 sec.

3.3 From 3D magneto-optical trap to magnetic trap

Our 3D MOT can cool atoms form 400 K to 250 μK in a few seconds - considerably colder than the Boomerang nebula [56], the coldest natural spot in our universe. When constructing the MOT, the goal is to maximize the number of trapped atoms. Larger beams are better for this purpose. We use beams $1''$ in diameter. We maximized the number of atoms in the MOT by adjusting the beam powers and power splittings, the laser detunings, the beam alignment and the magnetic field. The optimization stems from trade-offs between the capture velocity, trap stiffness, collisions, and scattering of light from the beams. In our MOT there is also a trade-off between the number of ^{87}Rb and ^{40}K atoms stemming from light-assisted collisions [57]. This trade-off is illustrated in Fig. 3.3, where a ^{40}K MOT is loaded during 31 sec and then a ^{87}Rb MOT is loaded in addition. As a result, the number of ^{40}K atoms decreases rapidly as that of ^{87}Rb increases. We thus load ^{87}Rb atoms during a short period, suffering minimum resulting loss of ^{40}K atoms. In addition, following [58], we shine the 2D MOT cell with blue light LEDs instantaneously increasing the vapor pressure and the loading rate considerably. This is not done constantly though, since all atoms will be removed from the walls, and the LEDs will cease to cause this desired effect. We thus operate the LEDs during 3 sec of ^{87}Rb loading.

Two σ_+ and σ_- counter-propagating beams of circularly polarized light illuminate the atoms in the chamber from three perpendicular directions. Each beam consists of the two merged cooler lasers of ^{87}Rb and ^{40}K . The beams from two of the perpendicular directions include in addition the two merged repump lasers of ^{87}Rb and ^{40}K . The lasers intensity and detuning are detailed in Tables 3.1 and 3.2. The 3D MOT is operated with two magnetic coils in an anti-Helmholtz configuration which create a magnetic field with a gradient of $10.6\frac{\text{Gauss}}{\text{cm}}$ along the coils axis. Additional Helmholtz configured coils are used to compensate for magnetic field from sources other than the MOT coils, such as that of earth. As an additional effort for reducing light-assisted collisions, we use a dark spot MOT [59]. We set a circular block 5 mm in diameter in the middle of the repump lasers to create the

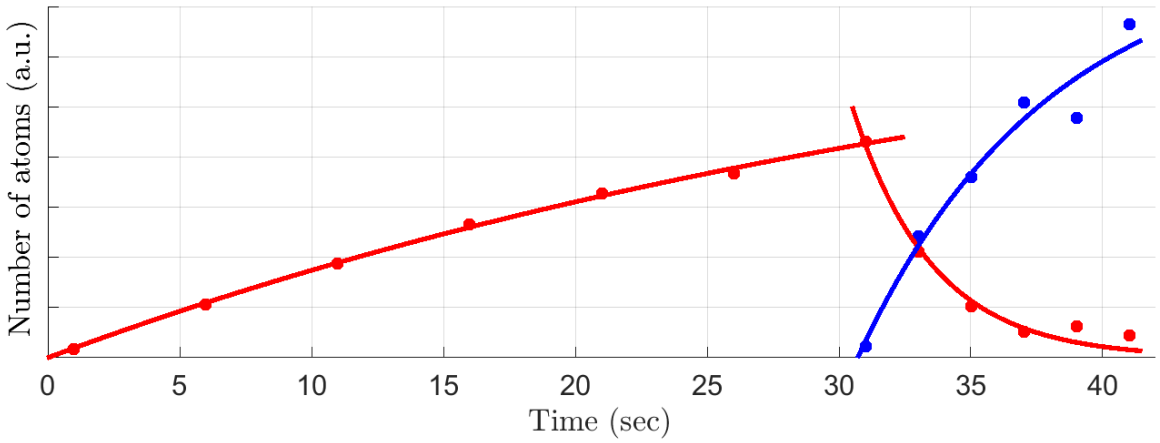

Figure 3.3: Number of ^{40}K (red) and ^{87}Rb (blue) atoms during 3D MOT loading. The numbers of each species are normalized separately, to plot them both on the same graph. A ^{40}K MOT is loaded during 31 sec and only then a ^{87}Rb MOT is loaded in addition. As the number of ^{87}Rb atoms increases, that of ^{40}K rapidly decreases. The solid lines are exponential fits. The rise-time of ^{40}K is 41 sec, that of ^{87}Rb is 7.2 sec, and the decay time of ^{40}K is 3.0 sec.

dark spot. This gave a factor of three improvement in the number of ^{40}K atoms in the 3D MOT.

In our 3D MOT we trap more than 10^9 ^{87}Rb atoms and a few 10^8 ^{40}K atoms in a sphere 2 mm in diameter at a temperature of $T = 250\ \mu$K. The atomic density is 2.4×10^{11} cm^{-3} for ^{87}Rb and a few 10^{10} cm^{-3} for ^{40}K . The phase space density is about $\Phi = n\lambda_{db}^3 = 10^{-6}$ for ^{87}Rb and 10^{-7} for ^{40}K . The atoms are in various states and collide at a rate of a few tens of Hz with a long lifetime of 10 sec.

The 3D MOT density is limited to a constant value due to radiation trapping [60]. Trapping more atoms will therefore make the MOT larger. This becomes problematic when trying to load the atoms to a magnetic trap, since the atoms pick up excess potential energy, resulting in an increased temperature. One way to minimize this drawback is to compress the MOT by increasing its magnetic field gradient, and adjusting the intensity and the detuning of the lasers [61]. When performing a Compressed MOT (CMOT), the goal is to minimize the MOT size without reducing the number of trapped atoms. We minimized the MOT size by abruptly changing the magnetic field gradient and the intensity and detuning of the lasers for

some time. We use a magnetic field gradient of $19.2\frac{\text{Gauss}}{\text{cm}}$, reduced intensities for all four cooler and repump lasers and ^{40}K repump detuned by -40 MHz $= -6.7\Gamma$ during 140 ms.

The effect of the CMOT is judged in terms of phase space reduction in the magnetic trap. The CMOT stage did not show a significant advantage for ^{87}Rb , while it doubled the phase space density of ^{40}K in the magnetic trap.

After the Doppler cooling stages we use a Polarization Gradient sub-Doppler Cooling (PGC) stage [62] aimed at minimizing the phase space density of the atoms, while not letting them fall too much, so they will not slosh after loading to the magnetic trap. When optimizing the PGC we need to start with a large capture velocity and end with a low final temperature. We thus gradually detuned the cooler lasers to final values detailed in Table 3.3, and reduced their intensity during the 4 ms PGC. The effect of the PGC is judged in terms of phase space reduction in the magnetic trap. The PGC increases the phase space density in the magnetic trap by more than three times. The PGC is highly sensitive to magnetic field and is thus used to improve the magnetic field cancellation in the 3D MOT chamber. PGC ends with about 10^9 ^{87}Rb atoms and 10^8 ^{40}K atoms at a temperature of $T = 70\ \mu$mK.

Table 3.3: Final laser beam detunings for PGC. The ^{87}Rb cooler is detuned from the $F = 2 \rightarrow F' = 3$ transition. The ^{87}Rb repump is detuned from the $F = 1 \rightarrow F' = 2$ transition. The ^{40}K cooler is detuned from the $F = 9/2 \rightarrow F' = 11/2$ transition. The ^{40}K repump is detuned from the $F = 7/2 \rightarrow F' = 9/2$ transition.

Laser		Detuning	
^{87}Rb	Cooler	-53.4 MHz	-8.8Γ
	Cooler	-18.7 MHz	-3.1Γ
^{40}K	Repump	-37.8 MHz	-6.3Γ

In order to trap the atoms in a magnetic trap we optically pump ^{87}Rb atoms to the $|F = 2, m_F = 2\rangle$ state and ^{40}K atoms to the $|F = 9/2, m_F = 9/2\rangle$ state, which are the high magnetic field field seeker states. For the optical pumping (OP) in our system we chose to use the $F = 2 \rightarrow F' = 2$ transition for ^{87}Rb and the $F = 9/2 \rightarrow F' = 9/2$ for ^{40}K , being robust in the sense the desired states are dark state of the OP lasers. The OP lasers frequencies are tuned to be resonant with the relevant transition and their intensities are chosen to minimize the OP duration. A magnetic field of about 0.5 Gauss parallel to the σ^+ polarized OP laser

beams is turned on right after the PGC stage to define a quantization axis. We use OP merged laser beams $1''$ in diameter of intensity 400 mW for ^{87}Rb and 105 mW for ^{40}K . The repump lasers are kept on during OP. We manage to pump more than 90% of the atoms to the desired states. Almost all of the remaining atoms end in other trappable states.

3.4 Quadrupole magnetic trap and transport

A quadrupole magnetic trap [63] is associated with a linear trapping potential. A cloud from a MOT is thus inherently mismatched for loading into such a trap and a reduction in the atoms phase space density is expected. The goal in loading the atoms to a quadrupole magnetic trap is to minimize phase space reduction by choosing an optimized trap magnetic field gradient [52]. We use the 3D MOT coils for the magnetic trap. We load the atoms using a trap with a magnetic field gradient of $58\frac{\text{Gauss}}{\text{cm}}$ along the coils axis. Although we optimized this stage, it suffers a loading efficiency of about 85% and heating to about 130 μK. The atoms have a lifetime of 10 sec in the MT.

In order to cool the atomic gas to quantum degeneracy evaporation is required, which takes a time longer than the lifetime in the 3D MOT chamber, limited by its pressure. We thus use a magnetic transport to move the atoms to the ultra-high vacuum science chamber. The MOT and science chambers are connected by a differential pumping tube 10 cm long and 8 mm inner diameter. The conductance of this tube is $c = 0.6\frac{\text{L}}{\text{sec}}$ - smaller than the both pumping rates of the MOT and science chambers pumps. The tube thus maintains a differential pumping between the chambers.

After loading the magnetic trap we adiabatically compress it by increasing its magnetic field gradient to $192\frac{\text{Gauss}}{\text{cm}}$ during 200 ms. We need to compress enough for the atomic clouds not to touch the walls of the differential pumping tube, and to avoid tight compression that will increase three-body collisions. The atoms are transported along 42 cm during 3 sec. The transport has an efficiency of 35% for ^{87}Rb and 60% for ^{40}K . It heats the cloud to about 500 μK.

3.5 Magnetic Quadrupole Ioffe Configuration trap (QUIC)

Using a plugged MT, we observed our system suffers from RF noise at frequencies between 0.5 kHz to few MHz. This noise is responsible for spin flips of atoms, which become considerable at late stages of the evaporation, considerably limiting the lifetime in the magnetic trap. Sympathetic cooling of ^{40}K by ^{87}Rb requires longer evaporation periods, due to a reduced inter-species collisional cross-section (Ramsauer-Townsend minimum [64]), and is incompatible with the atoms short lifetime in our MT. We thus designed and constructed a Magnetic Quadrupole Ioffe Configuration trap (QUIC). The bias field at the trap minimum Zeeman shifts the atomic energy levels making the RF noise in the lab far red-detuned from spin flip resonance, extending the lifetime in the trap.

The QUIC should fulfill the following:

- The magnetic field bias in the trap should be set to at least a few Gauss, in order to avoid the effect of the RF noise.
- The trap frequencies should be high enough (about 100 Hz on average) allowing a collision rate for efficient evaporation.
- The atomic cloud should be positioned far enough from the science cell wall.

For cold enough clouds, atoms in a QUIC trap will be confined by a cigar-shaped harmonic potential [52], where the angular trap frequency $\omega_\perp$ along the transverse directions scales as $\omega_\perp^2 \sim \frac{B'^2}{B_0}$. Here B' is (up to a constant) the axial gradient of the pure quadrupole field, and B_0 is the trap bias magnetic field. In practice we adjust the magnetic field bias B_0 by choosing the coil parameters and changing the currents in the MT and Ioffe coils, the Ioffe coil distance from the science cell and the current in the compensation coils. These degrees of freedom affect the trap frequencies as well as the trap center and the bias field, and thus need to be optimized mutually. Changes in the Ioffe coil position mainly affect ω_z and shift the trap center.

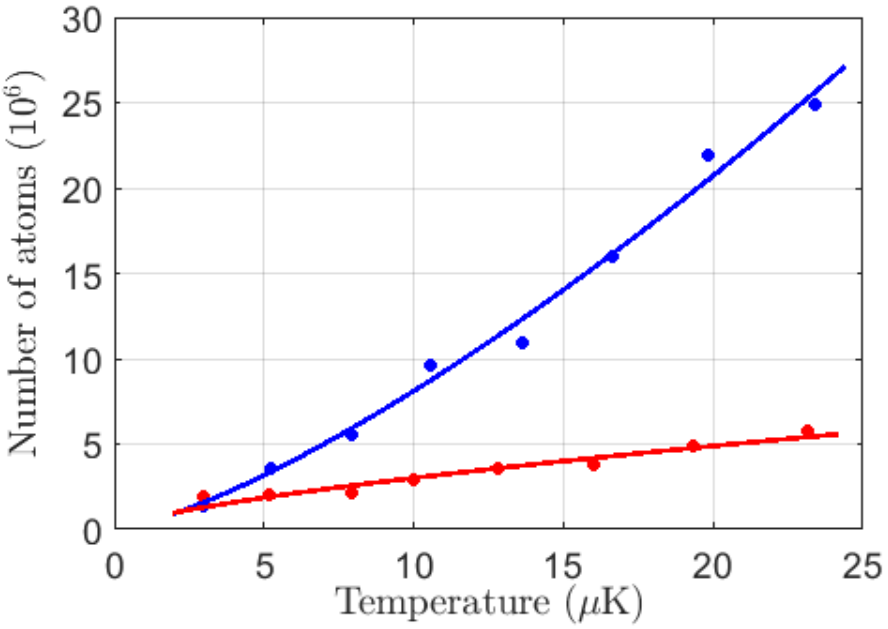

Figure 3.4: Final part of sympathetic cooling of ^{40}K (red) and evaporation of ^{87}Rb (blue) atoms in the QUIC. By fits (solid lines) we extract $\alpha = 0.7$ for ^{87}Rb and $\alpha = 1.4$ for ^{40}K . $\alpha = \frac{d\ln T}{d\ln N}$, where T is the cloud temperature and N, the number of atoms.

Our QUIC has typical trapping angular frequencies of $\omega_z = 2\pi \times 20$ Hz and $\omega_r = 2\pi \times 120$ Hz along the axial and radial directions, respectively. We trap 2×10^8 ^{87}Rb and 3×10^7 ^{40}K atoms in the QUIC having a bias of $B_0 = 5$ Gauss (measured by evaporation to various frequencies), a lifetime of 60 sec and angular trap frequencies of $2\pi \times (120, 120, 20)$ Hz. We then evaporate ^{87}Rb atoms by a radio frequency (RF) sweep, which sympathetically cools ^{40}K atoms during about 20 sec - see Fig. 3.4. The evaporation of ^{40}K is efficient, as quantified by the parameter $\alpha = \frac{d\ln T}{d\ln N}$ exceeding unity. ^{40}K ceases to further cool beyond the point where the number of atoms in each species becomes comparable. We achieve quantum degeneracy with both species of atoms with low repeatability, which we attribute to magnetic field fluctuations. When evaporating ^{87}Rb to near quantum degeneracy, the atoms end up with $T = 106\ \mu\text{K} \pm 31$ nK, which corresponds to magnetic field fluctuations of $\Delta B = 0.9$ mG (assuming $k_B \Delta T = \hbar \Delta\omega$, where $\frac{\Delta\omega}{\Delta B} = 2\pi \times 0.7 \frac{\text{MHz}}{\text{Gauss}}$). Along the evaporation we verified the states of the atoms stay pure by a Stern-Gerlach measurement.

3.6 Far-off resonance optical dipole trap

The trapping potential of a Far-off resonance optical dipole trap (FORT) is approximately insensitive to the trapped atoms state. We thus perform experiments in a FORT rather in a magnetic trap, keeping the atoms state as a degree of freedom. A FORT has further advantages of fast tunability, better stability and immunity to spin-flip-induced losses.

We use a crossed trap of two perpendicular beams of waists $w_{\parallel} = 150\ \mu$m and $w_{\perp} = 40\ \mu$m, of wavelength 1064 nm and total power of 10 W. We ramp the FORT adiabatically during 400 ms and then turn off the QUIC in 200 ms. We trap atomic clouds of up to $T = 8\ \mu$K with few percent loss in phase space density. The lifetime of atoms in the FORT is affected by the states of the atoms and by locking the trapping beams intensities. We use microwave (MW) STIRAP[1] to pump ^{87}Rb atoms to the $|F = 1, m_F = 1\rangle$ and RF STIRAP to pump ^{40}K atoms to the $|F = 9/2, m_F = -9/2\rangle$ ground states. We keep a constant magnetic field of few Gauss along the quantization axis. We measure the magnetic field by MW ^{87}Rb spectroscopy working on various transitions (see Fig. 3.5). This ability is important for future planned research, where we intend to measure shifts in such spectra indicating energy shifts associated to mediated interactions - see Chapter 5. Preforming Ramsey spectroscopy we recently managed to measure energy shifts with a precision of 3 Hz, which is satisfactory for the planned experiment according to theoretical prediction. The decoherence time in our measurement is 280 ms.

The atoms have a lifetime exceeding 90 sec, consistent with the pressure in the science chamber measured to be 10^{-11} Torr. We managed to evaporate the ^{87}Rb and ^{40}K clouds in the FORT getting a pure BEC of 1.5×10^5 ^{87}Rb atoms and 5×10^5 ^{40}K atoms at 170 nK ($T/T_F \approx 0.4$). A bimodal distribution typical of a BEC column density after time of flight is shown in Fig. 3.6.

[1] Stimulated Raman adiabatic passage [65].

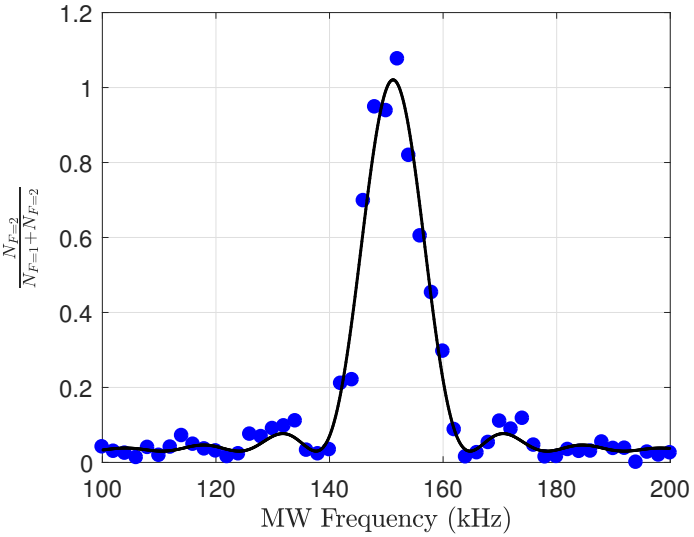

Figure 3.5: ^{87}Rb MW Rabi spectrum of the $|F=1,m_F=1\rangle \leftrightarrow |F=2,m_F=0\rangle$ transition. The normalized detection signal is monitored for 75 μs pulses on a ^{87}Rb cloud after 7 ms time of flight. The data fits (solid line) to a 6.8 kHz width. The resonance frequency corresponds to a magnetic field of 210 mG. $N_{F=1}$ denotes the number of atoms in $F=i$ states.

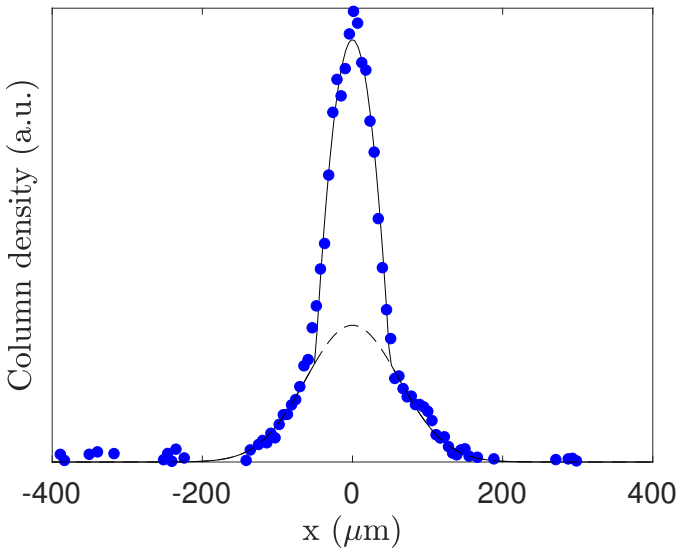

Figure 3.6: Column density of a ^{87}Rb BEC (blue dots) and a bimodal distribution fit (solid line) after 16 ms time of flight. The thermal fraction distribution is shown in dashed line. The cloud contains 1.7×10^5 ^{87}Rb atoms, has a condensate fraction of 17% and a temperature of 160 nK.

Chapter 4

Optomechanical Strain in a Cold Atomic Cloud

This experiment was inspired by early works on phase contrast imaging (PCI) of cold atoms [29, 66]. By multiple imaging of a single Sodium BEC realization, Ketterle showed that PCI is a non-destructive imaging technique, since no considerable absorption of the imaging light by the atoms is involved. Absorption imaging destructiveness was quantified in terms of the heating rate of the cloud due to absorption of photons and photon emission to a random direction. The results were consistent with a heating rate of twice the recoil temperature for each scattering event. PCI destructiveness was quantified in terms of the heating rate of the cloud due to the momentum transfet to the atoms steming from the slight change in the photons direction when passing through the cloud. The results showed PCI becomes even less destructive, since for a trapped cloud the velocity given to the atoms averages out during trap oscillations.

PCI is thus indeed non-destructive, but as Ketterle pointed out, when quantifying this statement - it is perturbative. The atoms do feel a force due to the imging process, though this force keeps the clouds center of mass intact and is also averaged during trap oscillations for in-situ measurements. Ketterle interpreted this though in terms of a dipole force acting on the atoms by the slightly deflected imaging light.

In our work we formulated a theory for this perturbation in terms of a force, which we call *electrostriction*, since it resembles shape changes of materials under the application of a static electric field[1]. We measured the effect of this force on a trapped cloud of cold ^{87}Rb atoms by imaging the strain on the cloud. We differentiated between electrostriction and other well-established light-atom forces, observed surprising results we do not fully understand and predicted implications of electrostriction of importance to cold atoms research. In particular, we show that this force cannot be explained in terms of a dipole force acting on the atoms by the deflected light. Our understanding could also settle a discrepancy between results and theory in other works. These results are published in Physical Review Letters [67]. We also gathered preliminary results aimed towards demonstrating electrostriction-induced pattern formation.

4.1 Observation of Optomechanical Strain

In this work we analyze and measure for the first time the optomechanical strain induced in a cold atomic cloud by a homogeneous laser beam far detuned from atomic resonance. We shine the beam on the cloud and directly observe the resulting strain after time of flight by absorption imaging. We show that this is a new kind of light-induced force acting on cold atoms. A saturation of the strain is observed, which depends only on the ratio between the momentum impulse applied to the atomic cloud and the initial momentum distribution width of the cloud. Possible implications for this new force are suggested, and, in particular, light-induced interaction tuning.

With respect to laser light far from resonance, an inhomogeneous atomic cloud behaves as a lens [29], as predicted by the optical Bloch equations. When a plane wave passes through the cloud, it acquires a position-dependent phase $\phi(\vec{r})$. If the phase is small, the Poynting vector direction changes [48] by an angle $|\vec{\nabla}_\perp \phi|/k_L$, where $\vec{\nabla}_\perp$ is the gradient along the two directions perpendicular to the laser beam propagation direction, and k_L, the wave number of

[1] This force is actually more similar to piezoelectricity than to electrostriction, since the sign of the force changes with the sign of the laser detuning. Even-though, we sticked to the initially chosen noise.

the beam. As a back-action, the atomic momentum changes in the opposite direction. The momentum change of the atoms is associated with the electrostriction force, which takes the form [Eq. (2.1.4)]

$$\begin{aligned} \vec{f}_{\rm es} &= \frac{\hbar\Gamma^2}{8\Delta}\frac{I}{I_s}\frac{\vec{\nabla}_\perp n}{n} = -\vec{\nabla}_\perp U_{\rm es} \\ U_{\rm es} &= -\frac{\hbar\Gamma^2}{8\Delta}\frac{I}{I_s}\ln\left(\frac{n}{n_0}\right), \end{aligned} \tag{4.1.1}$$

where n_0 is an arbitrarily chosen constant density that fixes the arbitrariness in defining a potential up to a constant, Γ, the width of the atomic transition, Δ, the detuning of the laser, I, its intensity, $I_{\rm s}$, the ^{87}Rb saturation intensity, and n, the local density of atoms.

This force acts only in the directions transverse to the beam propagation and is derived from a potential in the transverse directions that scales logarithmically with the density. It is a collective force in the sense that it acts only on atoms consisting of an inhomogeneous atomic cloud. The laser induces interactions between the atoms and the resulting force is independent of the number of atoms. Similar to the dipole force, changing the polarization can have a small effect of coupling different atomic states, which effectively changes I_s. The force scales as I/Δ, similar to the dipole force, and unlike other light-induced interactions predicted before [68, 69, 51], which are second order in atom-light coupling. For convex clouds it is repulsive for red detuned laser $\Delta < 0$, and attractive for blue detuned laser $\Delta > 0$, opposite to the dipole force.

In the experiment we typically trap 10^6 ^{87}Rb atoms in the $|F = 1, m_F = 1\rangle$ ground state of the $5^2S_{1/2}$ manifold at a temperature of $T = 400$ nK. Our crossed dipole trap has typical trap frequencies of $\omega_x = \omega_y = 2\pi \times 45$ Hz and $\omega_z = 2\pi \times 190$ Hz. The atomic cloud, when illuminated by a red detuned laser beam with $\Delta = -100$ GHz, is optically equivalent to a graded index lens of Gaussian profile $e^{-x^2/(2\sigma_z^2)-y^2/(2\sigma_y^2)-z^2/(2\sigma_z^2)}$. Its peak refractive index is $n_{\rm ref} = 1.0000093$ and its widths are $\sigma_x = \sigma_y = 22\ \mu$m, and $\sigma_z = 5.2\ \mu$m. To generate the electrostriction force we use a $\lambda = 780$ nm laser, $50 - 200$ GHz detuned from the $|F = 2\rangle \to |F' = 3\rangle$ transition. The beam is coupled to a polarization maintaining single

mode fiber and ejects with a waist of 1.1 mm. Under these parameters, the dipole force associated with the laser beam itself is suppressed by 10^{-3} compared to the electrostriction force, and the scattering probability is only a few percent. The dipole force that the light focused by the atoms exerts on the atoms is negligible. The electrostriction beam is shone from the $\hat{y}$ direction (see Fig. 4.1). The atomic cloud is optically extended ($\sigma \gg \lambda$), so a simple refractive media treatment is adequate. It is dilute ($nk^{-3} = 0.25$), so dipole-dipole inter-atomic interactions [70, 71] do not affect our experiment. To measure the force we apply a short pulse of duration τ_p right after releasing the cloud, and image the momentum distribution after a long expansion time [18 ms, Figs. 4.1(a)-4.1(c)] by absorption imaging along the $\hat{z}$ direction. Since the force is anisotropic, the cloud expands more in the transverse directions and gains an aspect ratio (AR) larger than unity. If the atoms do not move during the pulse (impulse approximation, $\tau_p \ll \omega^{-1}$) we can calculate the atomic cloud size σ along the transverse ($\perp$) and axial ($\parallel$) directions after time of flight. For a cloud with initial temperature T and after expansion time t,

$$\begin{aligned}\sigma_\perp &= \sqrt{\frac{k_B T}{m\omega_\perp^2}}\sqrt{\left(1-\frac{\hbar\Gamma}{k_B T}\frac{\Gamma}{8\Delta}\frac{I}{I_s}\omega_\perp^2 t\tau_p\right)^2+\omega_\perp^2 t^2}\\ \sigma_\parallel &= \sqrt{\frac{k_B T}{m\omega_\parallel^2}}\sqrt{1+\omega_\parallel^2 t^2}.\end{aligned} \tag{4.1.2}$$

After a long expansion time the aspect ratio $\sigma_\perp/\sigma_\parallel$ of the cloud reaches an asymptotic value,

$$\mathrm{AR}^2 = 1+\left(\frac{\hbar\Gamma}{k_B T}\frac{\Gamma}{8\Delta}\frac{I}{I_s}\omega_\perp\tau_p\right)^2 = 1+\left(\frac{\sigma_P^{\mathrm{es}}}{\sigma_P^{\mathrm{th}}}\right)^2, \tag{4.1.3}$$

where $\sigma_P^{\mathrm{es}} = \frac{\hbar\Gamma\sqrt{m}}{\sqrt{k_B T}}\frac{\Gamma}{8\Delta}\frac{I}{I_s}\omega_\perp\tau_p$ is the momentum distribution width of the electrostriction impulse, and $\sigma_P^{\mathrm{th}} = \sqrt{mk_B T}$ - the width of the initial cloud thermal momentum distribution.

Performing this experiment we observe that the electrostriction pulse neither changes the cloud size along the longitudinal direction nor the center of mass [Figs. 4.1(a)-4.1(b)]. This indicates that our experiment suffers no significant scattering and demonstrates the transverse nature of the optomechanical strain. This is more dramatically demonstrated

performing the same measurement on a BEC. In this case [Fig. 4.1(c)] the usually fragile bimodal distribution typical of a BEC along the axial direction is unaffected by the strong momentum impulse in the transverse directions. Similar results for pure condensates prove that the force acting on the atoms is different from that predicted in [51]. We nevertheless emphasize that our predictions in Eqs. (4.1.2) and (4.1.3) do not hold for a BEC, for which the equation has to be modified.

Applying an electrostriction pulse *in situ* generates a breathing mode oscillation, only in the transverse directions. This can be observed by letting the cloud evolve in the trap for some variable time, and imaging it after release [Fig. 4.1(e)]. The results in Fig. 4.1 did not depend on the laser polarization, in accordance with our theory. This observation also indicates that the interactions we induce between atoms are not dipole-dipole interactions.

We perform strain measurements after short electrostriction pulses for a large range of detunings $|\Delta| < 200$ GHz. The results (Fig. 4.3) are consistent with a $1/\Delta$ rather than a $1/\Delta^2$ scaling. This agrees with our prediction in Eq. (4.1.1) and rules out the scattering force and the forces in [69, 51], which scale as $1/\Delta^2$, as a source of the strain observed. Imaging the cloud a short time after the electrostriction impulse we observe the effect of the detuning's sign as well (Appendix C.2).

To qualitatively compare our observations to the theoretical prediction [Eq. (4.1.2)], we carefully calibrate our experimental parameters. In particular, we measured the spontaneous Raman transition rate between the $F = 1$ and $F = 2$ hyperfine states due to the electrostriction laser - see Fig. 4.2. The measured rate was in accordance with the rate calculated (see Appendix C.4) using the Kramers-Heisenberg equation [72, 73], given the independently directly measured laser intensity and detuning values, and the atomic parameters [74]. After calibration, the observed effect is roughly 2.5 times weaker than expected. As we currently do not have an explanation for this discrepancy, we scale our predictions by this factor when comparing results to theory throughout this work (Figs. 4.3-4.6). One way to settle this discrepancy is to directly measure the phase of the electrostriction laser beam using phase contrast imaging. We did not perform this measurement, since the phase shift imprinted on

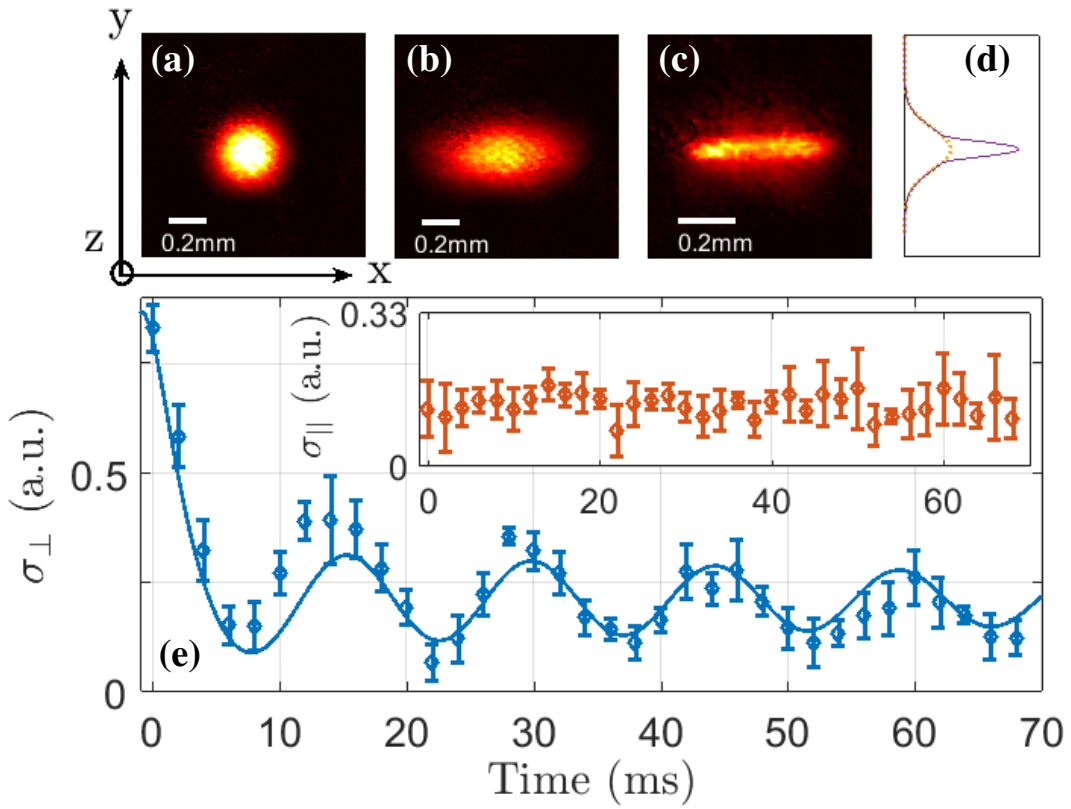

Figure 4.1: Strain measurements. Absorption image of a thermal cloud after long expansion times with (b) and without (a) an electrostriction pulse. The cloud aspect ratio changes from unity to 2.1. We used a laser beam shone along the $\hat{y}$ axis with intensity 8×10^3 mW/cm^2 ,detuning 47 GHz and pulsed for 0.5 ms. (c) A BEC after an electrostriction pulse and long expansion time. Even for a strong impulse and large aspect ratio the BEC remains partly condensed, showing a bimodal distribution in the axial direction (d). (e) Oscillations in the cloud size along one transverse direction (axial direction shown in inset) induced by an electrostriction pulse as a function of a variable waiting time in the trap after applying the pulse. A pure transverse breathing mode is observed, fitting to a decaying oscillation (solid line) of twice the trap frequency.

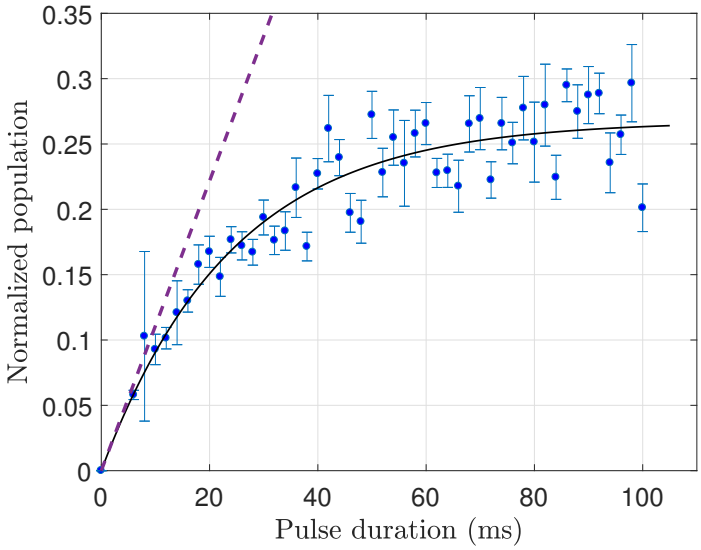

Figure 4.2: Spontanous Raman transition between $|F=1,m_F=1\rangle$ to any $|F=2,m_F\rangle$ hyperfine state, due to the π-polarized electrostriction laser of intensity $I = 7.6\times10^3\,\frac{\mathrm{mW}}{\mathrm{cm}^2}$ red detuned by $\Delta = 2\pi\times102$ GHz from the $|F=2\rangle\rightarrow|F'=3\rangle$ transition. The dashed line corresponds to an initial rate of 11.1 Hz.

the electrostriction laser beam [Eq.(2.1.2)] in our experiment is on the order of 10^{-3}, making it very challenging to detect. In addition, the refraction of the laser beam from the small cloud makes the light spread in an angle such that it hits the walls of our small science chamber, making detection further challenging. This measurement is planned to be performed in the lab of Gadi, Arnaud and Alex.

An example of a time of flight measurement is shown in Fig. 4.4. One can see that the fits to the data and the numerical calculation agree.

We further investigated the dependence of the electrostriction force on the cloud parameters: total number of atoms N and cloud size. We measured the aspect ratio, N, and the cloud size, while applying the same strain pulse on the cloud (Fig. 4.5 and inset). As seen, the measured AR is independent of N, as expected from Eq. (4.1.1). On the other hand, the effect shows a strong dependence on the atomic cloud size. Decreasing the cloud size makes the cloud a stronger lens, causing the beam to focus stronger and impart more momentum on the atoms.

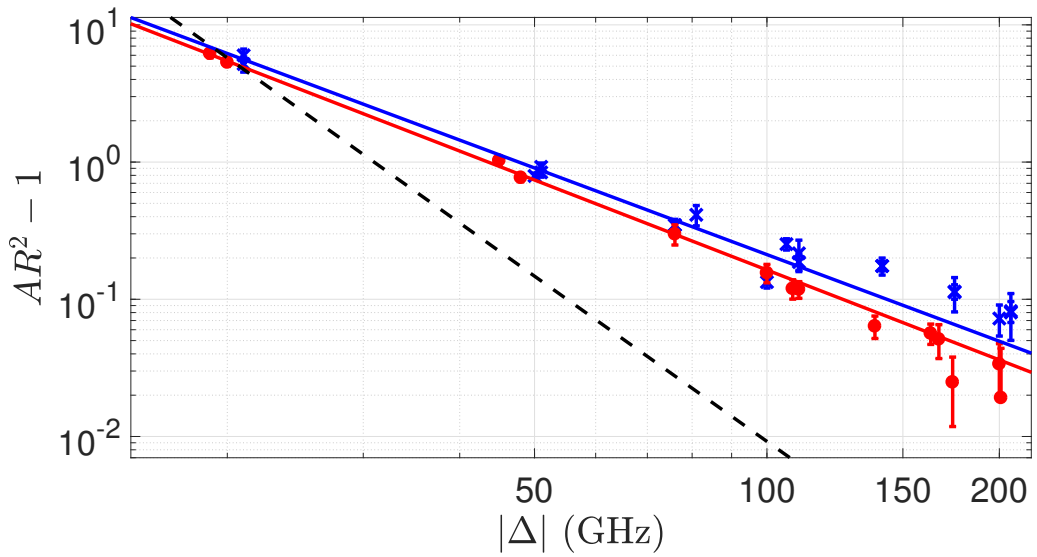

Figure 4.3: Scaling of strain with detuning Δ. A thermal cloud AR after an electrostriction pulse and free expansion, red circles (blue crosses), correspond to a red (blue) detuned electrostriction laser. Fits to the data (solid lines) indicate a scaling of the force as $1/\Delta^{\alpha}$, with $\alpha = 1.09(5)$ [$\alpha = 1.05(9)$] for the red (blue) detuned electrostriction laser. A prediction (dashed line) based on a force that scales as $1/\Delta^2$ is shown as well. The error in α corresponds to a 95% confidence level. We used a cloud with a temperature of 1.1 μK and a laser with intensity 1.1×10^4 mW/ cm^2, pulsed for 0.5 ms.

The dipole force might, in principle, cause dependence on the cloud size if the laser beam deviates from a plane wave, suffering intensity profile changes on length scales comparable with the cloud size. In order to avoid such situations, we work with a beam size about 100 times greater than the cloud size. We avoid speckles using a single mode fiber with a collimator and no other optical elements before the vacuum cell. We verified the absence of spacial sharp intensity changes by direct imaging of the beam. The strain we observed did not change after a slight misalignment of the beam, suggesting that indeed no significant local gradients appear. This shows that the observed cloud size dependence is not due to a dipole force of the electrostriction beam.

In order to verify the linearity of the electrostriction force strength with intensity I, we measured the strain as a function of growing optical power and different pulse durations and detunings. As seen in Figs. 4.6(a) and 4.6(b), linearity is indeed evident for low intensities. However, a clear saturation of the strain [Figs. 4.6(a)-4.6(c)] occurs at high intensities, for

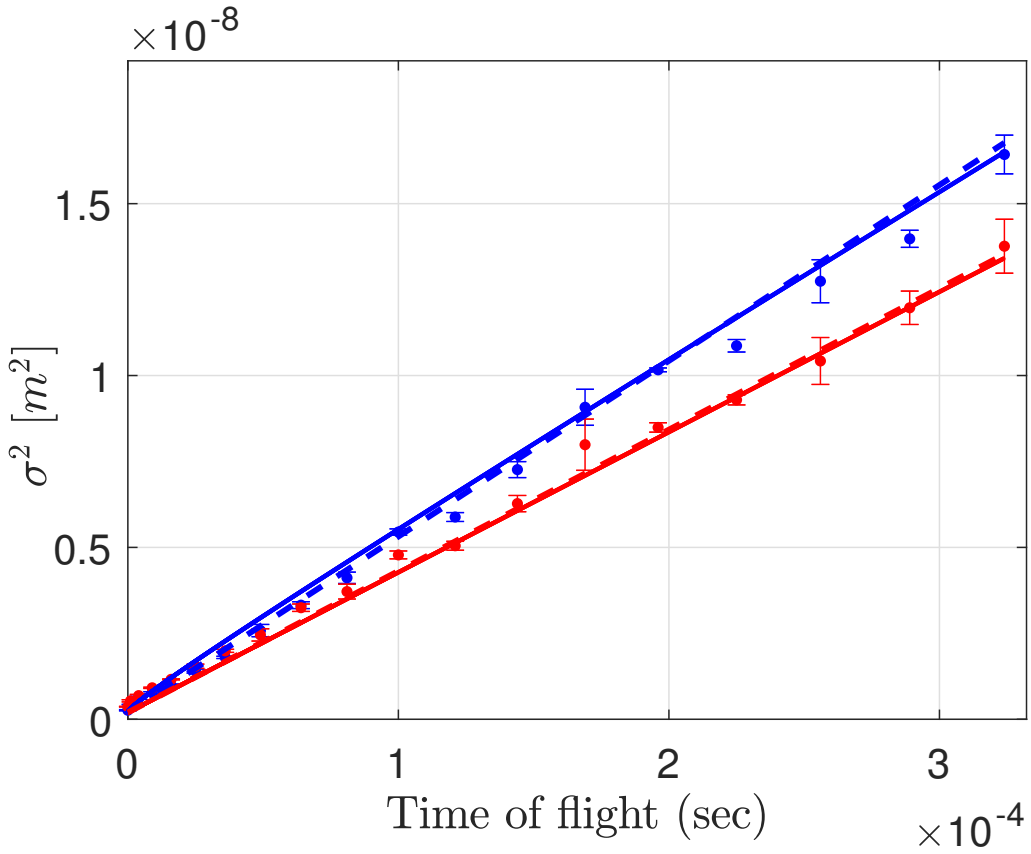

Figure 4.4: Time of flight measurement of a cloud pulsed after its release by an electrostriction laser beam. The cloud size σ is shown as a function of time along the longitudinal (red) and transverse (blue) directions. The fits to the data (solid lines) and the numerical calculation agree. We used a cloud of temperature $T = 430$ nK in a trap of trapping frequencies $\omega_x = \omega_y = 2\pi \times 73$ Hz and $\omega_y = 2\pi \times 293$ Hz. We pulsed it during $\tau = 0.2$ ms with a beam of intensity 6×10^3 mW/cm^2 and detuning of -100 GHz.

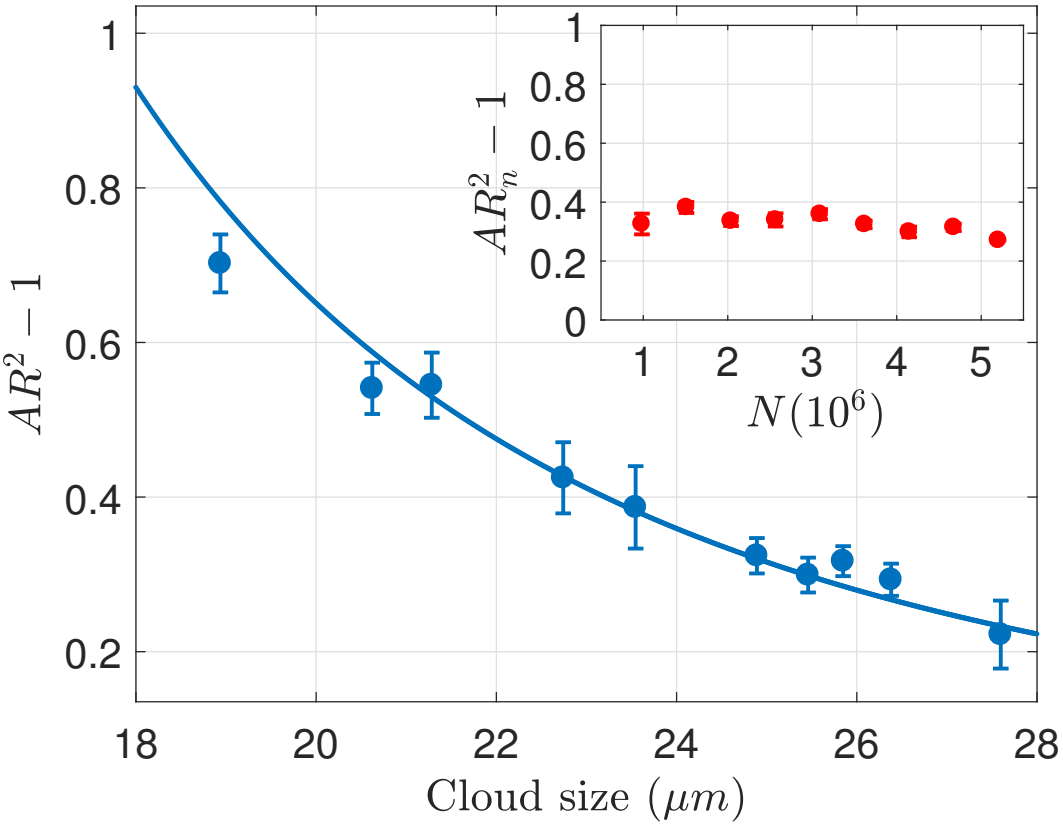

Figure 4.5: Strain for clouds of different sizes. Measured cloud aspect ratio after an electrostriction pulse and free expansion for different cloud sizes (circles), and the theoretical prediction (line, scaled strain). All data points correspond to thermal clouds besides the first one, which includes a small condensed fraction. Smaller clouds consist of fewer atoms, but the AR_n (normalized AR - see Appendix C.1) is independent of the number of atoms as can be seen in the inset. We used a laser with intensity 7.4×10^3 mW/cm^2 and detuning 73 GHz, pulsed for 0.25 ms.

various electrostriction pulse durations and detunings. We measured the dependence of saturation on the cloud temperature as well (not shown in Fig. 4.6), and found it appears to depend on the impulse applied to the atomic cloud $I\tau_p/(T\Delta)$. This is evident from the collapse of all data on a single curve as in Fig. 4.6. We note that the results presented in Figs 4.3 and 4.5 were performed for unsaturated strain.

The saturation of the effect stems neither from changes in the internal state of the atoms nor from expansion of the cloud during the pulse. Our pulses are considerably short (up to 1 ms) compared with the trap oscillation period of typically 20 ms and the spontaneous photon scattering rate of 20 Hz. We verified that there are no changes in the cloud density and internal state by imaging the cloud at short times and measuring the number of atoms in the $|F=1\rangle$ hyperfine state. The only evident change is the momentum distribution of the atoms, which should not affect the strain via our theory. As is clear from Fig. 4.6(c), saturation occurs when the atoms have accelerated to a momentum roughly equal to their initial thermal velocity spread, $\sigma_P^{\mathrm{es}} = \sigma_P^{\mathrm{th}}$.

The observation that lensing saturates close to $\sigma_P^{\mathrm{es}} = \sigma_P^{\mathrm{th}}$ is reminiscent of a classical version of Einstein's recoiling-slit gedankenexperiment [75, 76]. In this experiment an interference pattern of light that passed scatterers (slits) is dephased when the momentum imparted to the scatterers by the photons separates the scatterers in momentum space giving away the which-path information. In our experiment, lensing occurs due to coherent interference of light passing through different parts of the cloud. In an analogy to the above gedankenexperiment, the cloud would therefore cease to behave as a coherent lens after accumulating a momentum impulse σ_P^{es} comparable to their initial momentum distribution σ_P^{th}. I further elaborate on this analogy in Section C.5.

The bound on the electrostriction momentum given to the atomic cloud may prevent application of electrostriction for long times. For short times, the optomechanical strain has some interesting features of potentially practical importance (details in Chapter 2). An electrostriction laser beam applied to a BEC can effectively modify the inter-particle interaction strength at the mean-field level, mimicking the effect of a Feshbach resonance,

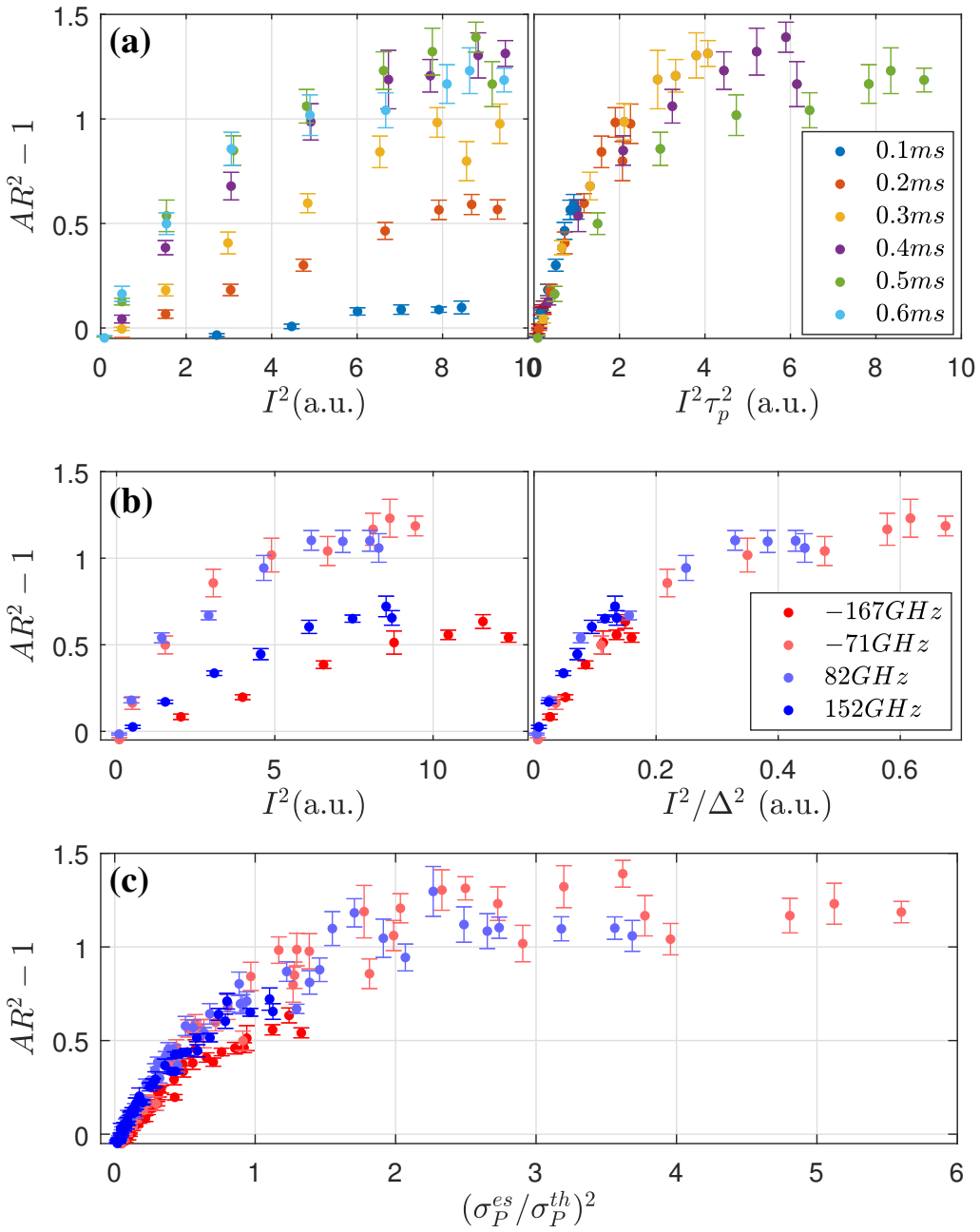

Figure 4.6: Strain saturation with electrostriction laser intensity I, detuning Δ and pulse duration τ_p. (a) Saturation with laser intensity I for different pulse durations τ_p (left graph). After scaling the results by τ_p^2 (right) they collapse to a single curve. (b) Saturation with laser intensity I for different detunings Δ (left graph). After scaling the results by Δ^2 (right) they collapse to a single curve. (c) When plotted as a function of the momentum impulse σ_P^{es}, all measurements collapse together. The laser intensity is changed between $0-9\times10^3$ mW/cm^2, the detuning Δ between $(-167)-(+152)$ GHz, and the pulse duration τ_p between 0.1 and 0.6 ms. σ_P^{th} is the width of the thermal momentum distribution prior to the electrostriction impulse.

without really changing the scattering length. Interaction tuning was used before [77] for short times using an optical Feshbach resonance. A BEC with attractive effective interactions induced by an electrostriction laser is unstable to spacial density modulations seeded by initial noise in the density profile of the cloud, as in nonlinear optical fibers [50]. An atomic cloud with repulsive effective interactions works to smoothen-out spacial density modulations. This can serve as an explanation to the unexplained red-blue asymmetry in [25]. The electrostriction potential [Eq. (4.1.1)] serves as a logarithmic nonlinearity, and thus a BEC under illumination can support stable solitons in any dimension [78] - a nontrivial feature [79, 80]. Finally, a thermal atomic cloud can be self-trapped by its own strain, resembling a bright soliton [81] in the transverse directions, incoherent and with arbitrary shape and size.

4.2 Towards electrostriction-induced pattern formation

In this section I will present unpublished results of our early research towards electrostriction-induced pattern formation. We observed a patterned atomic cloud density profile durring a time of flight measurement. Currently, we do not understand our observations. The observed patterns seem to stem from a mechanism different from that in our theoretical prediction in Section 2.5. We excluded a possible explanation that seemed most reasonable to me.

As mentioned in Section 2.5, a blue detuned laser will cause an electrostriction force, which will tend to amplify any modulation of an atomic cloud density profile. Such modulation amplification will in turn give rise to a stronger electrostriction force. This interplay creates a positive feedback mechanism for exponential growth of density modulations. The exponential growth rate depends on the density modulation, resulting in mode competition. As a result, the final pattern might be of a definite structure independent on the initial density modulation. Our prediction was derived for mode competition involved in pattern formation in a BEC, using a formal identity to the system of light propagation in an optical fiber with a Kerr nonlinearity [50]. We did not derive an analogous treatment for thermal clouds. Obser-

vation of pattern formation in-situ requires imaging high optical density clouds with high resolution. For these reasons we did not manage to properly perform in-situ measurements. During our search for the inward force on a cloud due to a blue detuned electrostriction laser beam, we unexpectedly observed density patterns. We initially attributed this result to a mechanism similar to the one described above.

We released the atomic cloud from a dipole trap, waited some time for free fall, pulsed the beam on the cloud and observed a resulting periodic density pattern after various periods by absorption imaging. The results of such a measurement and a simple time of flight measurement are compared in Fig. 4.7(a)-(b). One can see clear density profile fringes stretched along the electrostriction laser beam. In order to quantify the density modulation, the density profile has been fitted to a modulated Gaussian of the form $A\left(1+C\sin(k_f(x-x_0))\,\mathrm{e}^{-x^2/(2\sigma_x^2)-z^2/(2\sigma_z^2)}\right.$, where C quantifies the modulation contrast, k_f is the fringe spacial frequency, and x_0, a spacial fringe bias. The dynamics of the fringe contrast during time of flight is shown in Fig. 4.7.

In Fig. 4.8 the amplitude squared of the column density Fourier transform is plotted showing that the pattern spacial frequency is independent of the beam power, while its contrast increases with power until it saturates. We performed similar measurements on clouds of different temperatures as well (not shown).

In Fig. 4.9 the cloud size expansion during time of flight is monitored for a pulsed (blue and green dots, corresponding to the data in Fig. 4.7) and unpulsed cloud (red dots). One can see the cloud expands more in the transverse direction due to the electrostriction laser pulse.

The observed density pattern dynamics has the following characteristics:

- The fringe contrast gradually builds up after the laser pulse and fades away on a similar free fall time scale.
- The fringes appear at the same position for different realizations of the same experiment (spacially phase locked).
- The observed pattern appears for a red detuned laser beam as well as for blue detuned.

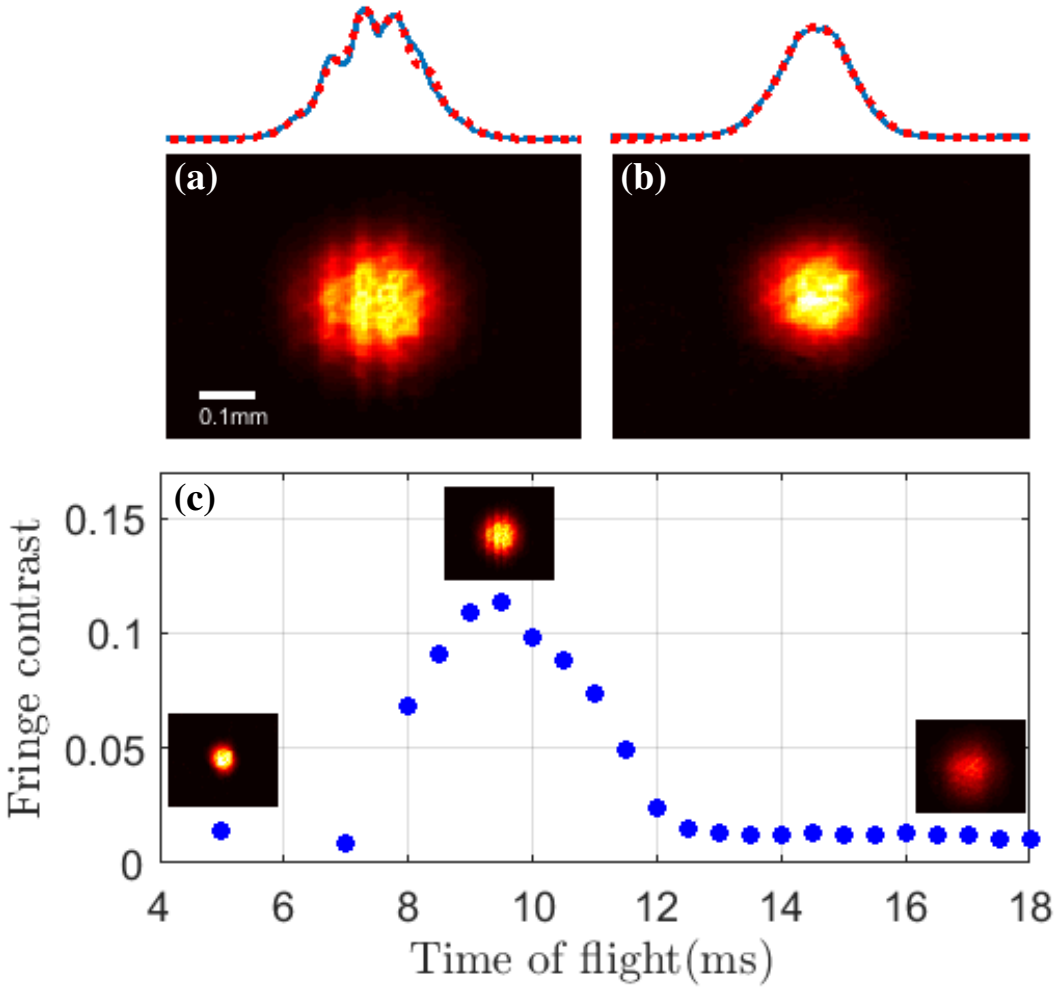

Figure 4.7: Pattern measurements. Absorption image of a thermal cloud with (a) and without (b) an electrostriction pulse, taken after 9.5 ms time of flight. Density line integrals are plotted above the cloud images (blue solid line) with a fitted modulated Gaussian (dashed red line). We used a laser beam shone along the $\hat{y}$ axis with intensity 8.4×10^3 mW/cm^2, detuning 100 GHz and pulsed for 1 ms after 7 ms time of flight. (c) Fringe contrast in cloud density profile during time of flight. The cloud profile develops fringes with a contrast increasing to 12% after the laser pulse and decreasing back after some time of flight. The contrast builds up and fades out on similar timescales. We used a cloud of 10^6 atoms at $T = 330$ nK trapped in a trap with frequencies of $\omega_x = \omega_y = 2\pi \times 54$ Hz and $\omega_z = 2\pi \times 230$ Hz. Each data point was calculated for an average over different realizations of images. Images taken after (before) the laser pulse were averaged over 21 (8) realizations.

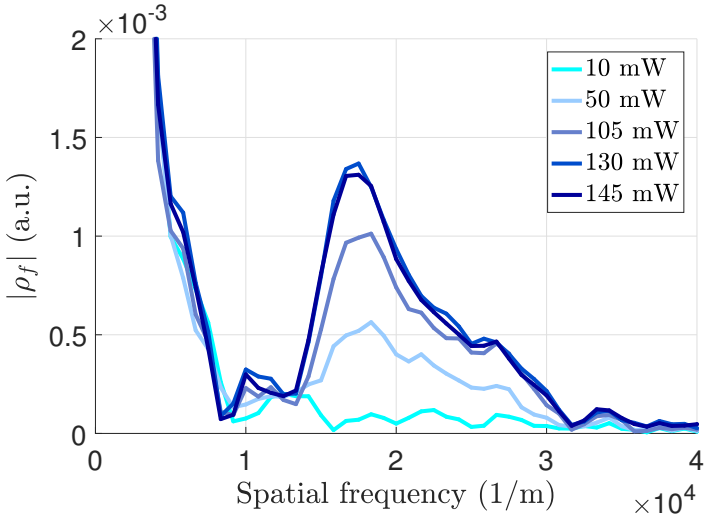

Figure 4.8: Pattern for different electrostriction laser beam powers. The graphs show the amplitude squared of the column density Fourier transform. The low frequency peak corresponds to the Gaussian cloud profile, while the higher frequency peak correspond to the modulation. The modulation spacial frequency is independent of the beam power, while its contrast increases with power till it saturates.

- The observed pattern is independent of the electrostriction laser beam polarization.
- The electrostriction laser beam intensity and the temperature of the cloud do not affect the pattern spacial frequency.

In addition, the cloud sizes (red dots) in Fig. 4.9 are larger than expected theoretically (dotted red line). The pulsed cloud gets larger during the pulse itself. We do not observe though any momentum distribution increase (the blue graph in Fig. 4.9 has the same slope as the red graphs).

The density profile spacial phase of the clouds analyzed in Fig. 4.7 did not change over 21 realizations. In this figure we thus used density profiles averaged over all realizations, resulting in a better signal to noise and demonstrating the fringes do not fade away due to averaging.

The above findings indicate that the observed pattern is not caused by the feedback mechanism described above. The predicted electrostriction force on the cloud in this experiment

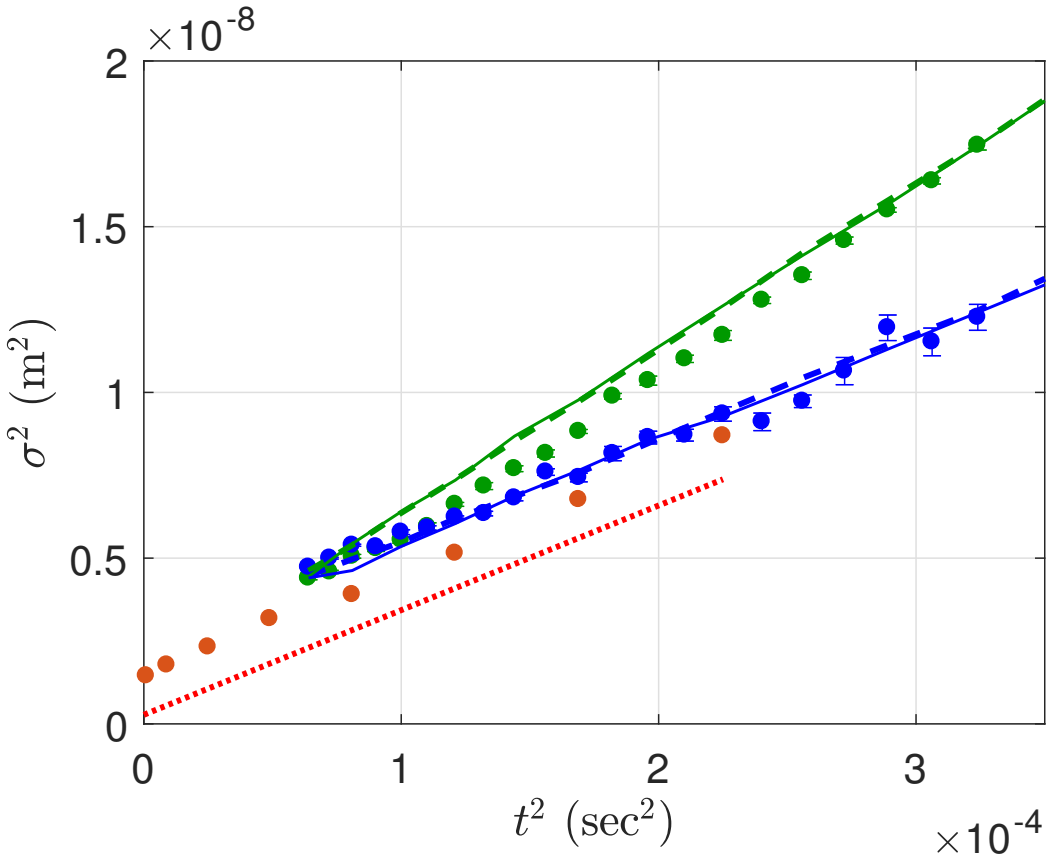

Figure 4.9: Time of flight measurement of a patterned cloud. Cloud size as a function of time for an unpulsed cloud along the transverse direction (red dots - two repetitions for each point) and the corresponding theoretical prediction (dotted red line). When pulsing the cloud during time of flight, the cloud size increases both along the longitudinal (blue dots) and the transverse (green dots) directions. Along the transverse direction, the cloud also gained a momentum kick. The pulsed cloud data was collected from 21 repetitions. The data can be fit assuming a large cloud (solid lines) or alternatively assuming our imaging system suffers a non-negligible point spread function (dashed lines).

is not strong enough to change the cloud density profile during the pulse itself, even if it has the modulation we observed, and thus positive feedback cannot enter the effect we observe. Given the electrostriction force in Eq. (2.1.4), which depends on the cloud density profile, the only explanation for the observed pattern should involve a cloud which already has a modulated density profile when pulsed by the electrostriction laser beam. Since our measurements were performed durring time of flight, we deduce such a modulation should originate from an in-situ modulation of the cloud density. Such a modulation can be hypothetically caused due to interference or reflections of our FORT beams. Our effort was thus to find a cloud with an in-situ modulated density, that will give rise to patterns similar to those we observed.

We used the phase space simulation mentioned in [67], which propagates the phase space density $n(x,p,t)$ in discrete time steps dt according to the evolution of a single particle of position x and momentum p under a force F

$$\begin{aligned} x(t+dt) &= x(t) + \frac{p(t)}{m}dt \\ p(t+dt) &= p(t) + F(t)dt \end{aligned} \tag{4.2.1}$$

by

$$\begin{aligned} n(x,p,t+dt) &= n(x - \frac{p}{m}dt, p - Fdt, t) \\ F &= \frac{\hbar\Gamma^2}{8\Delta}\frac{I(t)}{I_s}\frac{\vec{\nabla}_\perp n(x,t)}{n(x,t)} \\ n(x,t) &= \int_{-\infty}^{\infty} n(x,p,t)dp. \end{aligned} \tag{4.2.2}$$

Such a simulation is highly sensitive to numerical and coarse-graining noise, due to the dependence on density derivative and its nonlinearity. Numerical methods for overcoming these issues and in some cases ad-hoc methods were used. The simulation provided us with a non-general solution as a result of its inherent numerical instability. Changing the pulse duration, while keeping the total momentum impulse on the cloud constant, the simulation predicted independence of the result on the pulse duration in our working point, indicating

the effect is within the "impulse approximation". Assuming the impulse approximation significantly simplifies the treatment of this problem, allowing us to treat it analytically. We derived an analytical expression for the atomic cloud density profile dynamics in our experiment, hypothesizing in-situ cloud density modulation.

Consider a cloud of a modulated phase space density

$$\begin{aligned} n_0(x,p) &= n_0\left[1+d\cos(kx)\right]e^{-\beta H} \\ H &= \frac{p^2}{2m}+\frac{m}{2}\omega^2 x^2, \end{aligned} \tag{4.2.3}$$

so that the cloud density is a modulated Gaussian $n_0(x) = \int_{-\infty}^{\infty} n_0(x,p)dp =$
$= n_0\sqrt{\frac{2\pi m}{\beta}}\left[1+d\cos(kx)\right]e^{-\beta\frac{m}{2}\omega^2x^2}$. Allowing the cloud to freely expand during a time t_1, its phase space density will become $n_1(x,p) = n_0(x-t_1p/m,p)$, and the corresponding density will be

$$\begin{aligned} n_1(x) &= \int_{-\infty}^{\infty} n_0\left(x-t_1\frac{p}{m},p\right)dp = \\ &= n_0\sqrt{\frac{2\pi m/\beta}{b^2(t_1)}}e^{-\beta\frac{\frac{m}{2}\omega^2x^2}{b^2(t_1)}}\left[1+de^{-\frac{1}{b^2(t_1)}\frac{k^2t_1^2}{2m\beta}}\cos\left(\frac{kx}{b^2(t_1)}\right)\right] \\ b(t) &= \sqrt{1+\omega^2t^2}. \end{aligned} \tag{4.2.4}$$

When pulsing an electrostriction laser beam, the cloud will experience a force

$$\begin{aligned} F &= \frac{\hbar\Gamma^2}{8\Delta}\frac{I}{I_s}\frac{\frac{dn_1(x)}{dx}}{n_1(x)} = \\ &= -\frac{\hbar\Gamma^2}{8\Delta}\frac{I}{I_s}\frac{mx\beta\omega^2}{b^2(t_1)}+\Delta F \\ \Delta F &= -\frac{\hbar\Gamma^2}{8\Delta}\frac{I}{I_s}\frac{1}{b^2(t_1)}\frac{d\Omega\sin\left(\frac{kx}{b^2(t_1)}\right)}{e^{\frac{1}{b^2(t_1)}\frac{k^2t_1^2}{2m\beta}}+d\cos\left(\frac{kx}{b^2(t_1)}\right)}. \end{aligned} \tag{4.2.5}$$

The first term corresponds to the force in the absence of the initial modulation, while the ΔF term corresponds to the correction due to the initial modulation. If the pulse is applied during a short enough period τ, the phase space density right after it will become

$n_2(x,p) = n_1(x, p - F\tau)$. Allowing the cloud to freely expand during an additional time t_2, its phase space density will become $n_3(x,p) = n_2(x - t_2 p/m, p)$. The corresponding cloud density cannot be calculated analytically, but numerically.

Analyzing the pattern observed by the model described, I draw the following conclusions:

- The pattern observed in Fig. 4.7 is not predicted by the above calculation.
- Our model can in principle predict patterns with similar dynamics to those we observed. This occurs though only for a blue detuned laser[2] and in significantly different working points than in our experiment. Phase locking of the fringes will imply a phase locking of the in-situ modulation, which seems improbable if its due to noise or interference, which has interferometric sensitivity.

Note that our model cannot account for the pulsed cloud getting larger during the pulse itself.

The observation that the cloud size is measured to be larger than expected theoretically, indicates either that our imaging suffers an effective point spread function of width comparable to the cloud sizes we measure, or that for some reason the cloud is considerably larger than our prediction. We did not directly investigate these options. One should also notice the pulsed cloud gets larger during the pulse itself. This could have been explained by the scattering of the electrostriction laser light during these measurements (9% for each atom to scatter a photon), but it would be inconsistent with this scattering not increaseing the momentum distribution of the cloud, as seen from the blue graph, which has the same slope as the red graphs.

Ignoring the pattern observed and phenomenologicaly accepting that the cloud size increased during the electrostriction pulse, the underlying Gaussian cloud size dynamics can be explained by our model. Assuming our imaging suffers an effective point spread function of 34 μm width, the underlying Gaussian cloud size dynamics can be explained by our model

[2]There is a mathematical correspondence between ray tracing of light in an optical system and atomic cloud dynamics, which I do not cover in my thesis. The emergence of atom density fringes after applying an electrostriction laser pulse on a cloud modulated in-situ, corresponds to the emergence of an image by putting a lens after an object.

(dashed lines in Fig. 4.9). The electrostriction pulse increased the cloud size from 43 μm to 53 μm. The electrostriction effect was weaker than our theoretical prediction by a factor 2.6 - similar to the factor found in simpler experiments. Assuming the cloud is considerably larger than our prediction, say due to a highly non-harmonic potential, the underlying Gaussian cloud size dynamics can be explained by our model (solid lines in Fig. 4.9). To analyze this hypothetical option we considered a trap of angular frequency 2.3 times smaller than expected by former direct measurements. The electrostriction pulse increased the cloud size from 55 μm to 61 μm. The electrostriction effect was weaker than our theoretical prediction by a factor 2.25 - slightly smaller than the factor found in simpler experiments.

To summarize, we cloud not predict patters in the density cloud profile originating in any in-situ density modulation. Electrostriction pulse induced pattern revivals can be predicted by our model for working points differing considerably from ours. Due to our failure of explaining the observed pattern with our model, and due to the unique observed pattern properties - phase-locked fringes in particular, we speculate this is a result of some nonlinear effect we did not account for. This might relate to the observed saturation of the electrostriction force, implying the electrostriction force depends on the atoms velocity, in addition to the density profile.

Chapter 5

Summary and Outlook

In summary, I report the observation of optomechanical strain applied to ^{87}Rb thermal and condensed atoms when illuminated by an intense, far detuned homogeneous laser beam. We experimentally demonstrate the basic features of electrostriction, distinguishing it from the well-established scattering and dipole forces, and proving that it is a new type of force acting on cold atoms.

By the observed electrostriction characteristics, we point out that this force is distinct from theoretically predicted light-induced forces such as those discussed in [68, 69, 51] or collective forces measured in [82, 83]. The experimental results are in qualitative agreement with our theory. Based on our findings, electrostriction has the potential to be an important tool in cold atom experiments as it effectively induces interparticle interactions, which can be optically tuned.

There are aspects of this work, which we currently do not understand:

- We do not understand the microscopic origin of the electrostriction force.
- Our results repeatedly suffer a factor of about 2.5 in the electrostriction force compared to theory.
- We do not understand the observed saturation of the electrostriction force, though we have a useful analogy with the double slit experiment that might shed light on this problem in the future.
- We did not manage to observe the effect of electrostriction using a blue detuned laser, in a way which agrees quantitatively with our theory. We found only qualitative agreement. We hypothesize this is because of aberrations in the atomic lens and of the same unknown mechanism underlying electrostriction saturation.
- We do not understand the atomic density patterns we observed. We falsified the only explanation reasonable in our opinion.
- We did not manage to find indications for shifts in the trapping frequency we predicted in Section 2.6. We have hints this has some relation to the mechanism underlying electrostriction saturation.

These aspects should be studied in further research.

The system we constructed will serve as a generic research platform for ultra-cold many-body bosonic and fermionic systems, and in particular research on mediated inter-particle interactions.

The system we constructed is a generic research platform for ultra-cold many-body bosonic and fermionic systems. There are only few research groups using systems of quantum degenerate Bose and Fermi atomic mixtures. We have several research proposals using ^{87}Rb and ^{40}K . In the following I detail two major ones.

Inter-boson interactions mediated by Fermi sea excitations

Initiated by our research on electrostriction, we intend to proceed and investigate long range interactions between ^{87}Rb atoms mediated by particle-hole excitations of a ^{40}K Fermi sea [84], similar to RKKY interactions in solids [85–87]. This, as well as any other mediated interaction, was not measured yet on cold atoms, although several groups are currently working on the topic.

Using second order perturbation theory we calculated the shift in energy levels due to the RKKY interactions between the ^{87}Rb atoms. We intend to measure these energy shifts by MW spectroscopy. We recently performed our first MW Rabi spectroscopy on ^{87}Rb (see Fig. 3.5) as a starting point for checking our limits regarding Rabi frequency and magnetic field noise. We still need to look for the ^{87}Rb -^{40}K Feshbach resonance at 546.7 Gauss, quantify our magnetic noise and master using a multi-shutter camera for taking successive fast shots of atoms in different atomic state for both species.

A success in such a measurement might open a new fascinating possibility for research on fundamental theoretical questions about interacting systems. For instance, using Feshbach resonance, one might probe an interacting system along a crossover between the perturbative and non-perturbative regime. Not many theoretical tools are available for non-perturbative regimes.

Probing Fermi superfluid using a BEC

Fermi superfluids (FSFs) are theoretically understood mainly in the BCS and the BEC limits [88]. Understanding FSFs might allow engendering room-temperature superfluids and superconductors. The importance of such a possibility cannot be underestimated.

FSFs of cold Fermi gasses under Feshbach resonant magnetic field turn-out to be the highest high-T_c system known today. Several research groups probed different aspects of cold atoms FSFs, though they did not get access to the microscopic properties of the FSFs.

We propose using ^{87}Rb BEC as a probe for a ^{40}K FSF. We will Bragg-accelerate the BEC to a highly controlled velocity, let it collide with ^{40}K atoms, and measure the ^{87}Rb density profile after some time of flight. By analyzing such density profiles we can deduce microscopic properties not measured yet. In particular, we get access to the dispersion relation of the ^{40}K FSF, the two critical velocities associated with two types of the superfluid lowest excitations, and the chemical potential. Such measurements can provide new theoretical input to high-T_c physics.

Appendix A

Papers Published During my PhD

During my PhD I deduced most of my time to construction of the experimental setup as a generic research platform for many-body physics with ultra-cold bosons and fermions. I performed one experiment with published results and participated in a theoretical work [89] unrelated to my main physical interest, thus not detailed in this thesis.

1. N. Matzliah, H. Edri, A. Sinay, R. Ozeri, and N. Davidson, Physical review letters119,163201 (2017).

2. U. Levy, K. Yang, N. Matzliah, and Y. Silberberg, Journal of Physics B: Atomic,Molecular and Optical Physics51, 035401 (2018).

The first published work was cited in [90].

Appendix B

The Lasers in the System

Our system includes three External Cavity Diode Lasers (ECDL) and a DFB laser for cooling, trapping, optical pumping and imaging ^{87}Rb and ^{40}K atoms on a dedicated optical table (laser table). We use one DFB laser on a desk as the electrostriction laser, and one high power laser on the science table for the FORT.

B.1 The laser table

The lasers on the laser table are used for most of the manipulations and probing of the atoms. They are set on an individual table for the following reasons:

- The narrow spectral line of these lasers as required by the narrow atomic level widths, require mechanical and temperature stabilization.
- The lasers operate near atomic resonance, and thus stray light from them might cause severe atom loss.

Mechanical and temperature stabilization are achieved by a venting system which locks the temperature on this table to a fixed set-point of 21.3°C. The temperature of each laser is individually further locked using a temperature controller (TED200C, THORLABS). The

laser table is covered by curtains for thermal as well as optical isolation, while each laser diode is covered by a small plastic cover. Mechanical stabilization is achieved by floating the optical table and using rubber for mechanical isolation. The laser table is covered by curtains which were measured to absorb at least 99.99% of incident stray light. The curtains are inflammable and are not damaged by directly shining the few Watt laser beams we use. We shut laser beams by a shutter on the lasers table avoiding any stray light on the science table.

The manipulations on ^{87}Rb and ^{40}K atoms require a fair power at total and similar frequencies. We thus use four main lasers, which their power is split and frequencies shifted for the following roles for each atomic species:

- Cooler laser, which is used for cooling the atoms durring the MOT as well as PGC stages. This laser works on the cycling transition. It is also used for fluorescence imaging of the atoms in the MOT chamber.

- Repump laser, which is used for optically pumping the atoms that exit the cycling transition back to it. The repump laser is used during the MOT, PGC and absorption imaging stages. It is also used for optically pumping atoms in the lowest hyperfine state to a higher state for imaging.

- Spin polarization laser, which is used for optically pumping the atoms to a state of highest high-field seekers, before loading them to a magnetic trap. This laser is sometimes used for optically pumping atoms to a dark state of the imaging laser (*depumping*).

- Imaging laser, which is used for absorption imaging the atoms. This laser is resonant with the cycling transition.

The four main lasers are locked, amplified, split, detuned and injected into fibers. We name them after their most important roles: cooler and repump. The optical setup on the laser table is presented in Figure B.1. Three of the main lasers are locked using polarization

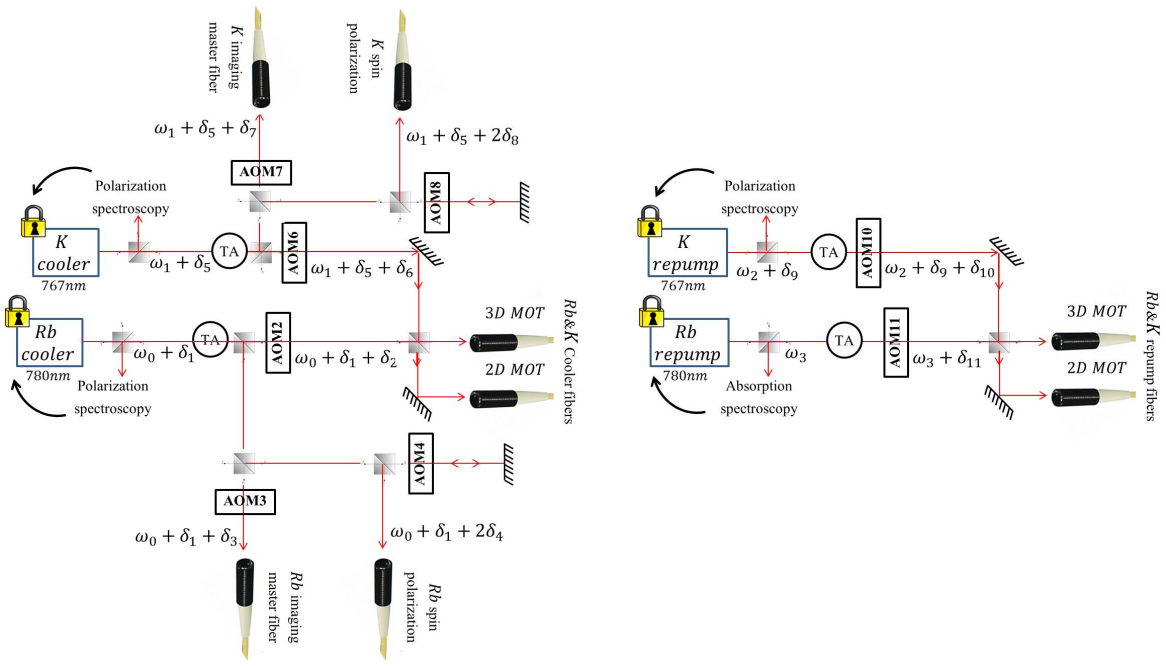

Figure B.1: The laser table setup. The lasers are locked, amplified, split, detuned and injected into fibers leading to the science table. TA stands for Tapered Amplifier. All beam splitters are polarizing. Laser angular frequencies are mentioned along the beam paths. ω_0 and $\omega_1 = \omega_2$ denote the ^{87}Rb $F = 2 \rightarrow F' = 3$ and the ^{40}K D2 transitions, respectively.

spectroscopy [91]. The ^{87}Rb repump is locked using saturated absorption spectroscopy [10] - a more sensitive method. The atomic level structure and the laser frequencies involved in our setup are presented in Figure B.2. The locked lasers are emphasized in the figure.

The polarization spectroscopy optics used for locking the ^{87}Rb cooler laser in plotted in Figure B.3. Using this spectroscopy method we measure an error signal associated with ^{87}Rb $F = 2 \rightarrow F'$ transitions and shown in Figure B.4, with which we lock the ^{87}Rb cooler laser to the ^{87}Rb $F = 2 \rightarrow F' = 3$ transition. When locking on this transition the pump and probe beams are resonant with atoms of the same velocity class, so that $\delta_1 = -(\delta_1 + 2\delta_{Lock}^{RbCooler})$, and the laser output is locked to $\delta_1 = -\delta_{Lock}^{RbCooler}$.

The saturated absorption spectroscopy optics used for locking the ^{87}Rb repump laser in plotted in Figure B.5. Using this spectroscopy method we measure an error signal associated with ^{87}Rb $F = 1 \rightarrow F'$ transitions and shown in Figure B.6, with which we lock the ^{87}Rb repump laser to the ^{87}Rb $F = 1 \rightarrow F' = 2$ transition. When locking on this transition the

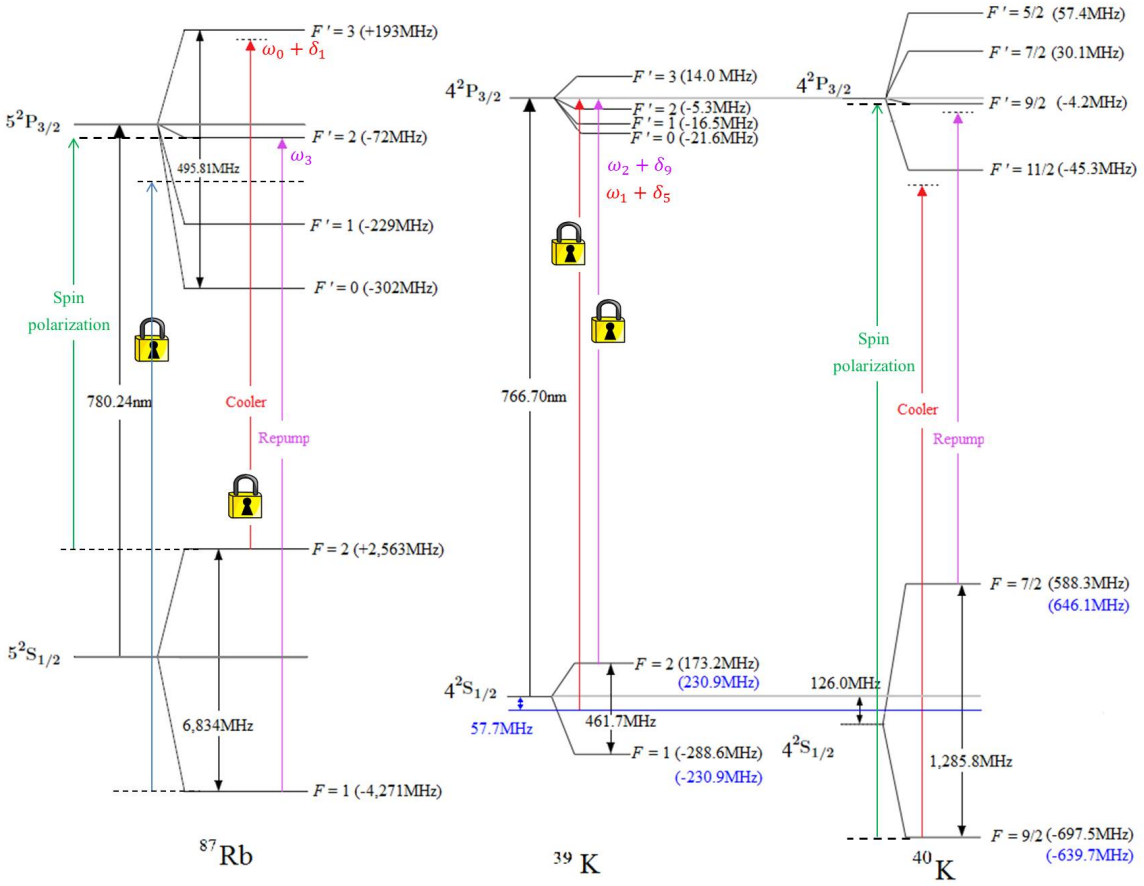

Figure B.2: Cooler and repump laser transitions shown on the energy levels of ^{87}Rb , ^{40}K and ^{39}K. In parentheses: hyperfine frequency shifts in MHz. The four locked diode lasers are presented. ω stands for the frequency of each transition, while δ stands for the detuning from ω, which changes during the sequence. The locked lasers have a lock sign on them.

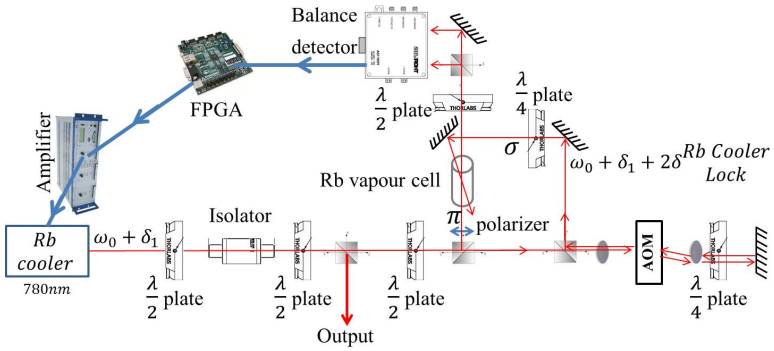

Figure B.3: Polarization spectroscopy optics used for locking the ^{87}Rb cooler laser. All beam splitters are polarizing. π denotes the linearly polarized probe beam. σ denotes the circularly polarized pump beam. Here only the pump beam is shifted by a double-pass through a 110 MHz acousto-optical modulator (1206C, ISOMET). Laser angular frequencies are mentioned along the beam paths. ω_0 denotes the ^{87}Rb $F = 2 \rightarrow F' = 3$ transition.

pump and probe beams are resonant with atoms of the same velocity class, so that the laser output is locked to $\omega_3 = \omega^{87Rb}_{F=1\rightarrow F'=2} - 2\pi \times 80$ MHz.

The polarization spectroscopy optics used for locking the ^{40}K cooler laser in plotted in Figure B.7. Using this spectroscopy method we measure an error signal associated with ^{39}K $F = 1 \rightarrow F'$ and $F = 2 \rightarrow F'$ transitions[1] shown in Figure B.8, with which we lock the ^{40}K cooler laser to the ^{40}K $F = 9/2 \rightarrow F' = 11/2$ transition. When locking on this transition the pump and probe beams are resonant with atoms of the same velocity class, so that $\omega_1 + \delta_5 + 2\delta^{KCooler}_{Lock} = \omega^{39K}_{\text{crossover}}$, and the laser output is locked to $\delta_5 = -2\delta^{KCooler}_{Lock} - 2\pi \times 68.25$ MHz. Here $\omega^{39K}_{\text{crossover}}$ is the crossover angular frequency between ^{39}K $F = 1 \rightarrow F'$ and $F = 2 \rightarrow F'$ transitions, and $\omega_1 - \omega^{39K}_{\text{crossover}} = 2\pi \times 68.25$ MHz. The polarization spectroscopy optics used for locking the ^{40}K repump is identical to that of the cooler. It is locked to the ^{39}K $F = 2 \rightarrow F'$ transitions.

[1] Two ^{41}K $F = 1 \rightarrow F'$ and $F = 2 \rightarrow F'$ signals are visible as well. The corresponding energy levels are not shown in Figure B.2

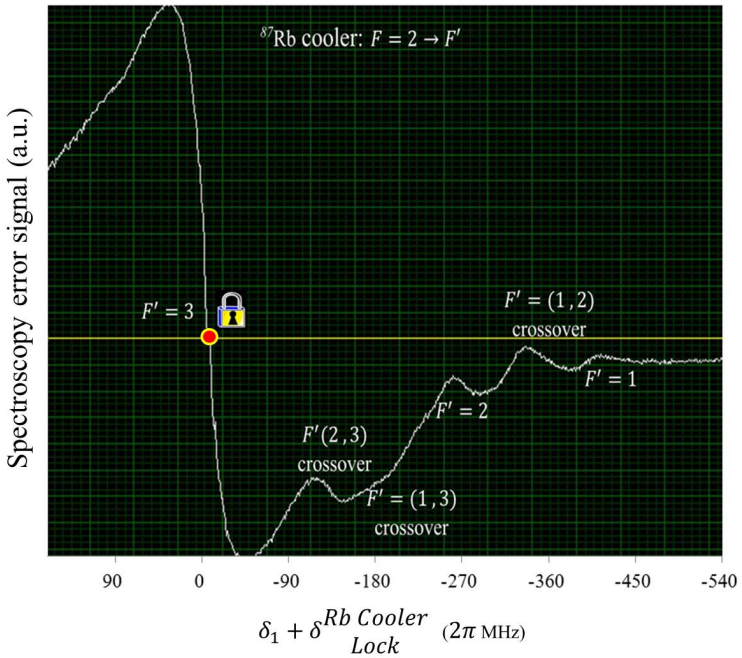

Figure B.4: Polarization spectroscopy error signal of ^{87}Rb $F = 2 \rightarrow F'$ transitions, used to lock the ^{87}Rb cooler laser. The ^{87}Rb $F = 2 \rightarrow F' = 3$ locking point is shown.

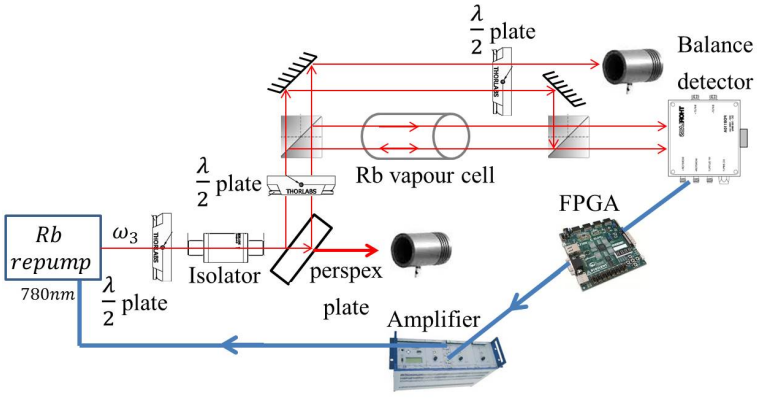

Figure B.5: saturated absorption spectroscopy optics used for locking the ^{87}Rb repump laser. All beam splitters are polarizing.

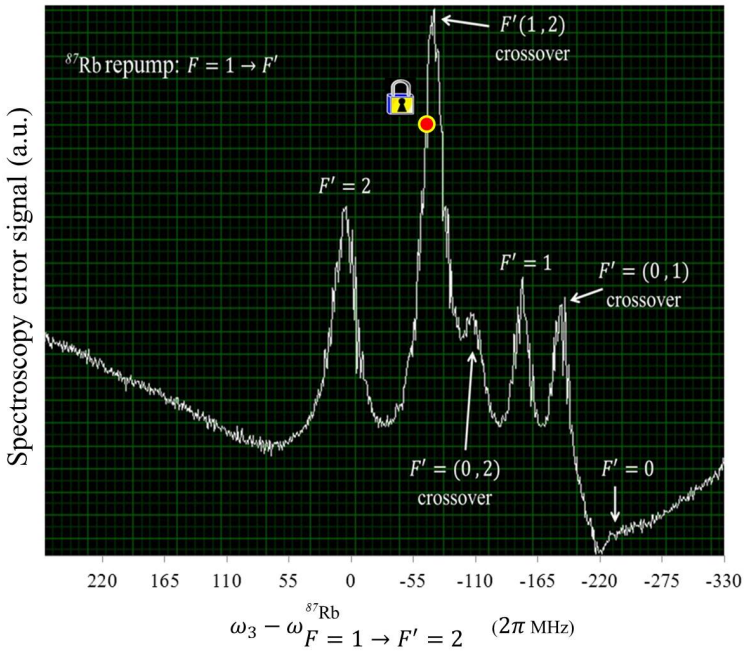

Figure B.6: saturated absorption spectroscopy error signal of ^{87}Rb $F = 1 \rightarrow F'$ transitions, used to lock the ^{87}Rb repump laser. The locking point is shifted by -80 MHz ^{87}Rb from the $F = 1 \rightarrow F' = 2$ transition denoted by $\omega^{^{87}Rb}_{F=1 \rightarrow F'=2}$.

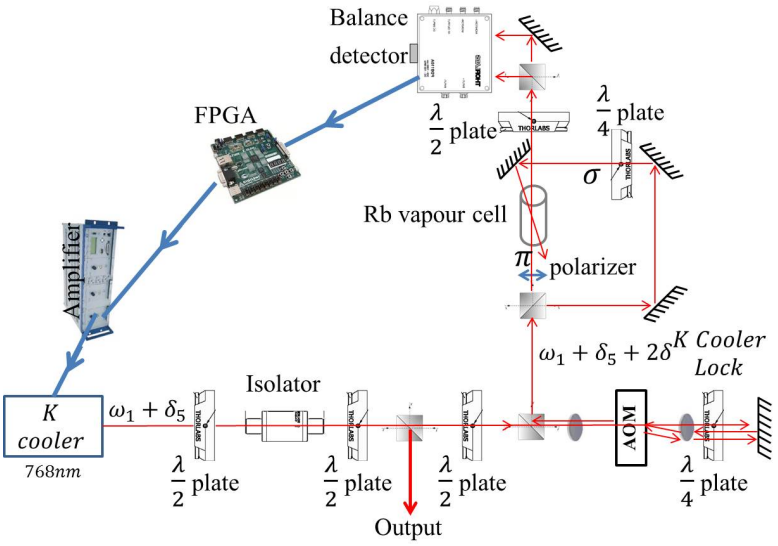

Figure B.7: Polarization spectroscopy optics used for locking the ^{40}K cooler laser. All beam splitters are polarizing. π denotes the linearly polarized probe beam. σ denotes the circularly polarized pump beam. Here both the pump and probe beams are shifted by a double-pass through a 250 MHz acousto-optical modulator (MT250-B100A0.5-800, AA OPTO-ELECTRONIC). Laser angular frequencies are mentioned along the beam paths. ω_1 denotes the ^{40}K D2 transition.

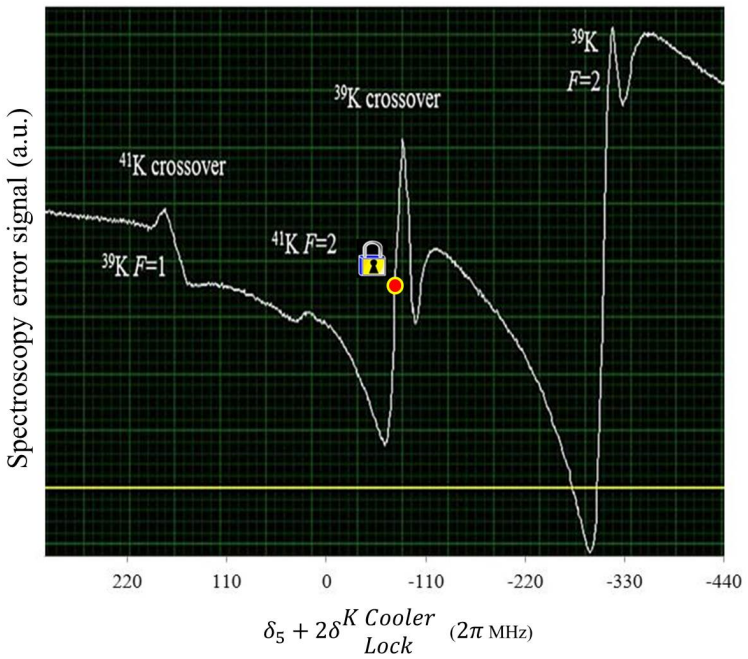

Figure B.8: Polarization spectroscopy error signal of ^{39}K $F = 1 \rightarrow F'$ and $F = 2 \rightarrow F'$ transitions, used to lock the ^{40}K cooler laser. The ^{39}K locking point is shown.

B.2 Other lasers

For a FORT we use a 42 W Mephisto MOPA, Coherent. For our experiment of measuring optomechanical strain on ^{87}Rb cloud we used a DFB laser (eagleyard EYP-DFB-0780-00080-1500-TOC03-000x) detuned from the ^{87}Rb D2 line without frequency locking, since the frequency is stable up to 0.5% of our typical detuning. The laser is amplified, spectrally filtered by a hot Rb vapour cell and fiber injected.

Appendix C

Electrostriction Supplementary Material

C.1 Experimental conditions and analysis specifics

The experimental parameters used in our measurements are summarized in Table C.1. All

Table C.1: Experimental parameters used in our measurements.

Parameter	Fig .1(b)	Fig .2	Fig .3	Fig .4
$N(10^6)$	1.2	3	1.5 - 4.5	2
$T(\ \mu\text{K})$	0.4	1.1	0.26 - 1.1	0.5
$I\left(\frac{\text{mW}}{\text{cm}^2}\right)$	8×10^3	1.1×10^4	7.4×10^3	$<9\times10^3$
$\Delta(\ \text{GHz})$	47	-200 - 200	73	-167 - 152
$\tau_p(\ \text{ms})$	0.5	0.2	0.25	<0.6
$\frac{\omega_{\text{trap}}}{2\pi}(\ \text{Hz})$	$(45,45,190)$	$(64,64,270)$	$(57,57,240)$	$(49,49,208)$

measurements were performed waiting a time of flight of about 18 ms. I note that pulsing the cloud *in situ* right before release or right after release does not affect the result.

While repeating the measurements in Fig. 2 for each detuning, the electrostriction laser intensity I and the cloud temperature T slightly fluctuate by a few percent. We monitor I by a photodiode and T by the clouds width along the longitudinal direction for each run. In Fig. 2 we thus plot the normalized AR^2-1 as the combination $(\text{AR}^2-1)\left(\frac{<I>}{I}\frac{T}{<T>}\right)^2$ in

the ordinate, where $< I >$ and $< T >$ are the average laser intensity and cloud temperature respectively. This slightly affected the fit parameter α (see Fig. 2) by only a few percent.

Although clearly excluding the scattering force as responsible to the observed strain, the results in Fig. 2 slightly disagree with our theoretical prediction. We attribute this to systematic errors, presumably resulting from the long total time needed for data collection, and the fact the detuning is tuned manually.

Regarding Fig. 3, changing the number of atoms N, while keeping a constant cloud size (or equivalently temperature T) is not straightforward, since the evaporative cooling of the atoms is affected by the number of atoms involved via the collision rate [1]. We thus varied both N and T and plotted (Fig. 3 inset) the normalized $\mathrm{AR}_n^2 - 1$ as the combination $(\mathrm{AR}^2 - 1)\left(\frac{T}{T_0}\right)^2$ in the ordinate, where $T_0 = 540$ nK is a typical cloud temperature corresponding to a cloud size of 20 μm. We omitted all data points in the inset having less than 3×10^5 atoms, which suffer larger errors due to low signal to noise ratio. We omitted all data points in the inset having temperatures less than 0.8 μK in order to avoid condensates. The data points were clustered into ten bins.

A typical spontaneous photon scattering rate for our electrostriction laser is 80 Hz for a laser of power 150 mW (peak intensity 8×10^3 $\frac{\mathrm{mW}}{\mathrm{cm}^2}$) and 100 GHz detuning. For a pulse time of 0.2 ms, only 2% of the atoms will recoil on average. The ratio between the dipole potential of the electrostriction laser,

$$\begin{aligned} U^{es}_{\mathrm{dipole}} &= -\frac{m}{2}\omega^2_{\mathrm{dipole}} x^2 \\ \omega^2_{\mathrm{dipole}} &= \frac{2}{m w_0^2}\frac{\hbar\Gamma^2}{4\Delta}\frac{I_0}{I_s} \end{aligned} \tag{C.1.1}$$

[1] We could have changed N independently by other means, such as pumping some of the atoms from $F = 1$ to $F = 2$ and remove them by resonant illumination. Such methods might rise questions by skeptics though, such as regarding the effect of such a procedure on the remaining atoms.

and the electrostriction potential,

$$\begin{aligned} U_{\text{es}} &= -\frac{\hbar\Gamma^2}{8\Delta}\frac{I_0}{I_{\text{s}}}\ln\left(\frac{n}{n_0}\right) \\ n &= n_0 e^{-\frac{U_{\text{ext}}}{k_B T}} \\ U_{\text{ext}} &= -\frac{m}{2}\omega_{\text{x}}^2 x^2 \end{aligned} \tag{C.1.2}$$

along $\hat{x}$ is

$$\frac{U_{\text{dipole}}^{es}}{U_{\text{es}}} = \frac{2k_B T}{\frac{m}{2}\omega_{\text{x}}^2 w_0^2}. \tag{C.1.3}$$

Here m is the atoms mass, $w_0 = 1.1$ mm, the electrostriction laser beam waist, I_0, the laser's peak intensity, and $\omega_x = 2\pi \times 45$ Hz, the trap angular frequency along $\hat{x}$.

For a cloud of temperature $T = 400$ nK, we get $U_{\text{dipole}}/U_{\text{es}} = 1.6 \times 10^{-3}$. These calculations demonstrate the dipole force of the electrostriction laser and scattering from it are avoidable in our experiment.

Having a nonisotropic Gaussian density profile, the cloud behaves as a lens with aberrations and astigmatism. The paraxial focal length of the cloud along $\hat{x}$ is $f_x = 934$ mm. The distance from the cloud where the Fresnel number becomes unity along $\hat{x}$ is $L_x = 0.6$ mm. The cloud thus behaves more as a diffractive element than a refractive one. Notice that the length scale for changes in the electrostriction beam intensity profile is $L_x/\sigma_x = 28$ times larger than the cloud size. This illustrates that the cloud fulfills the "thin lens approximation" allowing us to optically analyze it considering only phase imprinting. As another result from this, the dipole force acting on the cloud, resulting from the intensity gradient of the laser beam after lensing in the cloud, is suppressed - 10^{-2} times weaker than the measured electrostriction force in a typical case. This can be seen by simulating the electrostriction beam propagation by a split-step Fourier method, and calculating the dipole force due to the beam intensity changes for a typical cloud - see Fig. C.1. In Fig. C.2 the a zoom out of the same results is presented, showing that the diffraction from the small cloud clearly dominates the focusing effect in the far field. In addition for being negligible, the dipole force should push the cloud mainly towards the beam propagation direction. No such longitudinal force

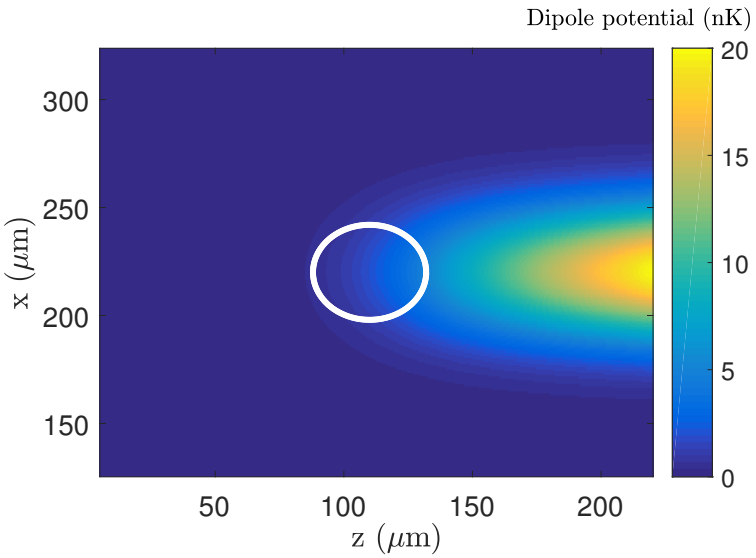

Figure C.1: Electrostriction beam dipole potential in nK. The cloud is situated at the center of the plot. A white circle of diameter 2σ, where σ is the width of the cloud Gaussian profile, represents the cloud. The beam is initially a plane wave and propagates to the right along $\hat{z}$. The plot shows the potential in a plane crossing the cloud center.

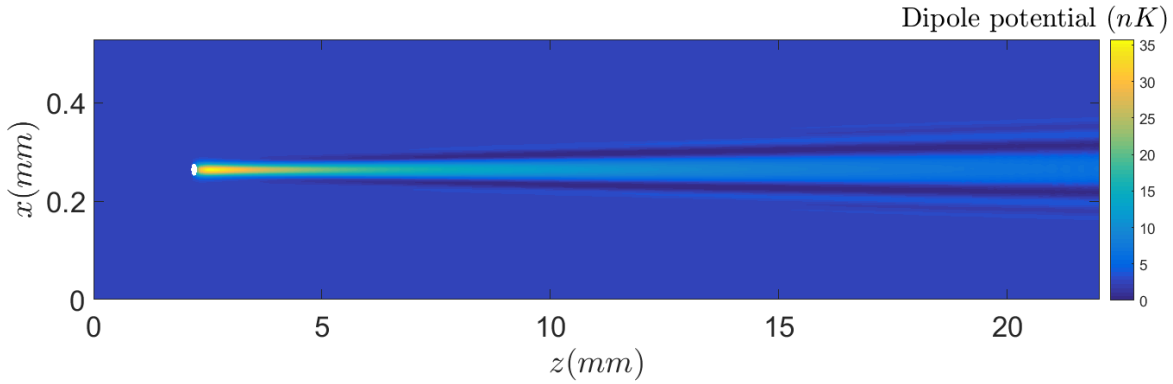

Figure C.2: Electrostriction beam dipole potential in nK. The cloud is denoted by a (highly elongated) white circle of diameter 2σ, where σ is the width of the cloud Gaussian profile. The beam is initially a plane wave and propagates to the right along $\hat{z}$. The plot shows the potential in a plane crossing the cloud center.

was observed in our measurements. I note the dipole force due to lensing scales as $1/\Delta^2$, while the electrostriction force scales as $1/\Delta$.

The electrostriction force itself is not pure transverse. The force will have a longitudinal component $\sigma_x/f_x \sim 10^{-5}$ weaker than its transverse component, and thus highly suppressed.

Another force one can think of that can act on the atomic cloud is due to radiation pressure of electrostriction light that is back reflected from the cloud. We ignored back reflection when deriving the electrostriction force in Section 2.1. Since the peak refractive index of our clouds are typically $n_{ref} - 1 = 10^{-5}$, the intensity of the back reflected light is limited by the Fresnel coefficient to $R = \left|\frac{n_{ref}-1}{n_{ref}+1}\right|^2 \approx 10^{-10}$ of the incident intensity. Here I considered a steep refractive index step and on-axis reflection for simplicity, while in practice the effect of back scattering is further suppressed. A cloud of size $\sigma = 22\ \mu$m in a beam of intensity $I = 10^4$ mW/ cm^2 will feel a power of $P = I\pi(\sigma/2)^2 = 0.38\ \mu$W. During a pulse of $\tau = 1$ ms, as many as $N_\gamma = \frac{\tau P}{\hbar\omega_L} = 1.5 \times 10^9$ photons will hit the cloud, while only $RN_\gamma < 1$ photons will be back reflected on average. Here ω_L is the laser angular frequency. This will transfer 10^{-7} recoil to each atom in a cloud of 10^6 atoms, a highly negligible effect.

C.2 The sign of detuning effect on the strain

The method presented in the manuscript is inert to the electrostriction laser beam detuning sign for long time of flight [see Eq. (4.1.3)]. In principle, imaging the atoms after a short time of flight can reveal the difference between a blue and a red detuned electrostriction laser beam. For a typical working point one needs to image the cloud after about 1 ms suffering a trade-off between the strength of the effect and the time window for observing it. This also poses a challenge to our imaging system due to the large optical density of the cloud, and limited resolution. We thus modified the method releasing the cloud from the trap, allowing it to freely expand for 6 ms, pulsed it during 1 ms, let it continue expanding freely for some variable time of flight, and imaged it - see Fig. C.3. This way the cloud is already large when imaged and the effect lasts for a few ms. A red detuned laser pulse exerts a momentum kick

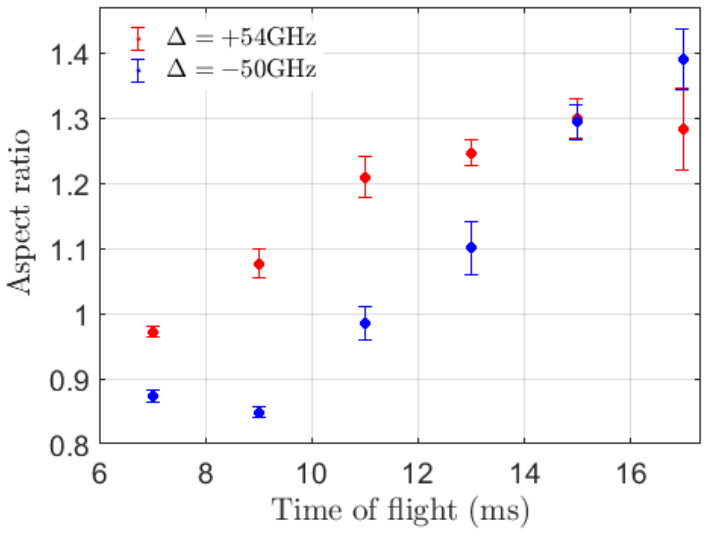

Figure C.3: Comparison between the atomic cloud aspect ratio evolution for a red (red dots) and a blue (blue crosses) detuned laser beam pulse. The cloud is released from the trap, allowed to freely expand for 6 ms, pulsed during 1 ms, continue expanding freely for some time of flight, and imaged. A red detuned beam makes the cloud to expand in the transverse direction. A blue detuned beam makes the cloud to shrink in the transverse direction and then expand.

outwards, making the cloud expand in the transverse direction and its aspect ratio to exceed unity. A blue detuned laser pulse exerts a momentum kick inwards, making the cloud shrink in the transverse direction and its aspect ratio to drop below unity. After the cloud shrinks, it expands again and the aspect ratio exceeds unity.

This demonstrates the effect of the detuning's sign, though comparison to simulation shows the cloud's aspect ratio should have dropped much lower for blue detuning. This relates to our observation of saturation in which after gaining a momentum impulse comparable to that of the thermal momentum distribution width, the cloud ceases to further gain momentum. In the measurement here the cloud after time of flight ceases to gain considerable momentum. In both cases, induced position-momentum correlations in phase space prevents additional momentum transfer. In the first case, position-momentum correlations are induces by electrostriction, while in the second case it is induced by free expansion.

C.3 Multilevel atom treatment

The theoretical treatment presented in this work considered the susceptibility of two-level atoms. The susceptibility of ^{87}Rb atoms take a different value, which depends on the laser polarization.

For a multi-level atom, the susceptibility takes the form

$$\chi = n\frac{\frac{i}{\hbar}|\mu|^2}{\varepsilon_0(i\Delta+\Gamma)}. \tag{C.3.1}$$

Scattering atoms from $|F=1,m_F=1\rangle$, the electric dipole moment takes the form

$$|\mu|^2 = \Sigma_{F',m'_F}\left|\Sigma_q a_q \left\langle F=1,m_F=1\right| er_q \left|F',m'_F\right\rangle\right|^2, \tag{C.3.2}$$

where q is the circular decomposition index, a_q is defined by the decomposition $\vec{r}\cdot\hat{\varepsilon} = \Sigma_{q\in\{0,\pm1\}}a_q r_q$, $\hat{\varepsilon}$ being the laser polarization unit vector. Note that the sum over m_F and q reduces to a single sum due to selection rules. The polarization of a general elliptically polarized laser propagating along $\hat{y}$ toward atoms quantized along $\hat{z}$, as in our experiment, can be parameterized as $\hat{\varepsilon} = \cos\phi\hat{z} + \sin\phi e^{i\theta}\hat{x}$. We thus recognize $a_0 = \cos\phi$ and $a_{\pm1} = \frac{\sin\phi e^{i\theta}}{\sqrt{2}}$. Plugging all matrix elements [74] in Eq.(C.3.2) in terms of the reduced matrix element (RME) gives,

$$\begin{aligned} |\mu|^2 &= \frac{1}{3}\mathrm{RME}^2 \\ \mathrm{RME} &= \left\langle J=\frac{1}{2}\right|\left|\left|er\right|\right|\left|J'=\frac{3}{2}\right\rangle = 3.584\times10^{-29}\ \mathrm{C\cdot m}. \end{aligned} \tag{C.3.3}$$

Notice the susceptibility is independent of the laser polarization. Furthermore, it takes the same value as for the cycling transition for a linearly polarized laser

$$|\mu^{\pi\text{-pol}}_{\text{cycling transition}}|^2 = \frac{1}{3}\mathrm{RME}^2. \tag{C.3.4}$$

I note this simple result is valid for elliptically polarized laser propagating perpendicular to the quantization axis. For instance, a laser propagating parallel to the quantization axis will induce a polarization-dependent effect.

This proves we can treat our atoms as two-level systems using the cross section $\sigma_0 = 1.938 \times 10^9$ cm^2, or equivalently the saturation intensity $I_s = 2.503 \frac{\text{mW}}{\text{cm}^2}$, of a linearly polarized laser working on the cycling transition.

C.4 Spontaneous Raman transition rate

We measured a spontaneous Raman transition rate of $\Gamma^{\text{exp}}_{|i\rangle\to|f\rangle} = 11.1$ Hz between the $|i\rangle = |F=1, m_F=1\rangle$ to any $|f\rangle = |F=2, m_F\rangle$ hyperfine state due to the π-polarized electrostriction laser of intensity $I = 7.6 \times 10^3 \frac{\text{mW}}{\text{cm}^2}$ (total power of $P = 145$ mW) red detuned by $\Delta = 2\pi \times 102$ GHz from the $|F=2\rangle \to |F'=3\rangle$ transition (Fig. 4.2). The rate of photon scattering events, in which an atom initially in state $|i\rangle$ ends up in state $|f\rangle$, is given by the Kramers-Heisenberg formula [72, 73],

$$\Gamma_{i\to f} = g^2\Gamma \left| \frac{a^{(1/2)}_{i\to f}}{\Delta} + \frac{a^{(3/2)}_{i\to f}}{\Delta - \Delta_f} \right|^2 . \tag{C.4.1}$$

Here, $g = \frac{E\mu}{2\hbar}$, $E = \sqrt{\frac{2I}{c\varepsilon_0}}$ is the laser-beam electric field amplitude, c, the speed of light, ε_0, the vacuum dielectric constant, and
$\mu = |\langle 2P_{3/2}, F=3, m_F=3 | \vec{d}\cdot\hat{\vec{\sigma}}_+ | 2S_{1/2}, F=2, m_F=2\rangle|$, where $\vec{d}$ is the electric dipole operator. The effective amplitude
$a^{(J)}_{i\to f} = \Sigma_q \Sigma_{e\in J} \langle f|\vec{d}\cdot\hat{\vec{\sigma}}_q|e\rangle\langle e|\vec{d}\cdot\hat{\vec{\sigma}}_k|i\rangle / \mu^2$ is the sum over amplitudes of scattering through all levels, $|e\rangle$, in the ^2P_J manifold, Δ is the laser detuning from the $^2S_{1/2} \to ^2P_{1/2}$ transition, and $\Gamma = 2\pi \times 6.0666$ MHz is the radiative linewidth of the excited states in the ^2P manifold [74].

In our case, we use detuning Δ up to few hundreds of GHz from the $|F=2\rangle \to |F'=3\rangle$ transition. We can thus neglect the $J = 3/2$ term in Eq. (C.4.1) for all working points.

The matrix element μ can be written in terms of the reduced matrix element (RME - see Eq. (C.3.3) above),

$$\mu = \left\langle F' = 3, m'_F = 3 \right| \vec{d} \cdot \hat{\vec{\sigma}}_+ \left| F = 2, m_F = 2 \right\rangle = \sqrt{\frac{1}{2}} \text{RME}. \tag{C.4.2}$$

In our case of a π-polarized laser,

$$\begin{aligned} \Sigma_{mF} \left| \Sigma_e \left| f \right\rangle \vec{d} \cdot \hat{\vec{\sigma}}_q \left| e \right\rangle \left\langle e \right| \vec{d} \cdot \hat{\vec{\sigma}}_k \left| i \right\rangle \right|^2 &= |\text{RME}|^4 \cdot \text{CG} \\ \text{CG} = \left| -\sqrt{\frac{1}{8}} \times -\sqrt{\frac{1}{12}} + \sqrt{\frac{5}{24}} \times \sqrt{\frac{1}{20}} \right|^2 + \left| -\sqrt{\frac{1}{8}} \times \sqrt{\frac{1}{24}} + \sqrt{\frac{5}{24}} \times \sqrt{\frac{1}{40}} \right|^2 + \\ \left| -\sqrt{\frac{1}{8}} \times \sqrt{\frac{1}{8}} + \sqrt{\frac{5}{24}} \times \sqrt{\frac{1}{120}} \right|^2 . \end{aligned} \tag{C.4.3}$$

All Clebsch-Gordan coefficients were taken from [74]. Plugging all values in Eq. (C.4.1) we obtain $\Gamma^{\text{theory}}_{|i\rangle \to |f\rangle} = 15.0$ Hz agreeing with the experimental value up to 36%. This result combined with our independent measurements of all laser and atoms parameters, convinces us we have reasonable control over the experiment parameters.

C.5 Analogy between saturation of electrostriction and the double slit experiment

In this section I show that in the recoiling double slit experiment, the effect of interference wash-out persists in the classical limit. The quantum limit of this system considers one photon, which momentum change accompanied to scattering by a slit is large compared to the uncertainty in the momentum distribution of the slit itself. The classical limit considers many such photons, where each of them get a momentum change small compared to the uncertainty in the momentum distribution of the macroscopic slit. The accumulated momentum delivered to the slits by all the photons together is though not small.

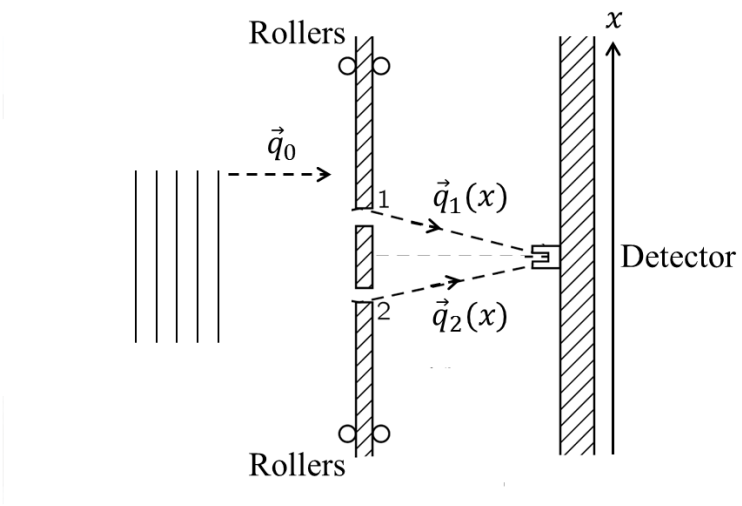

Figure C.4: Sketch of the recoiling double slit experiment. An incident photon of momentum $\vec{q}_0$ enters two slits and then hits a detector, which can be positioned along the $\hat{x}$ axis. After passing through slit i, the photons momentum will become $\vec{q}_i(x)$. The excess momentum of $\vec{q}_0 - \vec{q}_i(x)$ is delivered to slit i, which starts moving along the $\hat{x}$ axis on rollers.

Our system of recoiling atoms seems to realize a classical version of the recoiling double slit experiment, so the derivation in this section suggests a way to understand the observed saturation of the electrostriction force in terms of wash-out of the interference involved in the lensing of atomic clouds.

The recoiling double slit experiment is sketched in Fig. C.4. It considers N photons of wave number vector $\vec{q}_0$ propagating towards a wall with two slits, which are free to move on frictionless rollers along the $\hat{x}$ axis. Denoting the state of the first and second slits by $|I\rangle$ and $|II\rangle$ respectively, the initial state of the system is $\left|\{\vec{q}_0\}_{m=1}^N\right\rangle \otimes |I\rangle \otimes |II\rangle$. After the first photon is scattered by the slits, the state of the system becomes $\left|\{\vec{q}_0\}_{m=2}^N\right\rangle \otimes \int dx \left(|\vec{q}_1(x)\rangle \otimes e^{i\Delta\vec{q}_1(x)\hat{x}_1}|I\rangle \otimes |II\rangle + |\vec{q}_2(x)\rangle \otimes |I\rangle \otimes e^{i\Delta\vec{q}_2(x)\hat{x}_2}|II\rangle\right)$, where $\Delta\vec{q}_i(x) = \vec{q}_i(x) - \vec{q}_0$, and $\hat{x}_i$ is the position operator of slit i. This state can be reformulated as $\left|\{\vec{q}_0\}_{m=2}^N\right\rangle \otimes \int dx \sum_{m=1}^2 \binom{2}{m} \left(|\vec{q}_1(x)\rangle \otimes e^{i\Delta\vec{q}_1(x)\hat{x}_1}\right)^{2-m} \left(|\vec{q}_2(x)\rangle \otimes e^{i\Delta\vec{q}_2(x)\hat{x}_2}\right)^m |I\rangle \otimes |II\rangle$. By successive application of the above argument, one can convince himself that if all N photons pass though

the slits, the state of the system becomes:

$$|\psi\rangle = \int dx \sum_{m=1}^{N} \binom{N}{m} \left(|\vec{q}_1(x)\rangle \otimes e^{i\Delta\vec{q}_1(x)\hat{x}_1}\right)^{N-m} \left(|\vec{q}_2(x)\rangle \otimes e^{i\Delta\vec{q}_2(x)\hat{x}_2}\right)^{m} |I\rangle \otimes |II\rangle \quad \text{(C.5.1)}$$

After N photons passed the slits, the state of the photons can be described in terms of a density matrix ρ by tracing-out the slits degrees of freedom parameterized by the momenta k_i of slit i, $\rho = tr(|\psi\rangle\langle\psi|) = \int d\vec{k_1} d\vec{k_2} \left\langle \vec{k}_1, \vec{k}_2 | \psi \right\rangle \left\langle \psi | \vec{k}_1, \vec{k}_2 \right\rangle$. The integral over $d\vec{k_1} d\vec{k_2}$ is taken only over momenta along the $\hat{x}$ axis, to which the motion of the walls is confined. For simplicity I consider the initial state of the slits to be coherent states of uncertainty σ_k in the momentum distribution slit wave function $\langle k|I\rangle \propto e^{-(k/\sigma_k)^2}$ and $\langle k|II\rangle \propto e^{-(k/\sigma_k)^2 + ikd}$, where d is the distance between the slits. This allows calculating

$$\begin{aligned} &\left\langle \vec{k}_1, \vec{k}_2 | \psi \right\rangle = \\ &= \int dx \sum_{m=1}^{N} \binom{N}{m} \left(|\vec{q}_1(x)\rangle\right)^{N-m} \otimes \left(e^{i\Delta\vec{q}_2\cdot\hat{x}d} |\vec{q}_2(x)\rangle\right)^{m} \Omega_{(N-m)\Delta\vec{q}_1 - \vec{k}_1} \Omega_{m\Delta\vec{q}_2 - \vec{k}_2} e^{-ik_2 d} \end{aligned} \quad \text{(C.5.2)}$$

where

$$\Omega_{m\Delta\vec{q}-\vec{k}} = \left\langle \vec{k} \right| \left(e^{i\Delta\vec{q}(x)\hat{x}_1}\right)^{m} |I\rangle \propto e^{-\frac{\left(m\Delta\vec{q}(x)-\vec{k}\right)^2}{\sigma_k^2}}. \quad \text{(C.5.3)}$$

One can see that if $|\Delta\vec{q}_i| \gg \sigma_k$, we can approximate $\Omega_{\vec{k}} \approx \delta\left(\vec{k}\right)$, and for each integer m in the sum of Eq. C.5.2 only $\vec{k}_1 \approx (N-m)\Delta\vec{q}_1$ and $\vec{k}_2 \approx m\Delta\vec{q}_2$ will contribute to the integration over $d\vec{k_1} d\vec{k_2}$, so that $\rho \approx \sum_{m=1}^{N} |\phi_m\rangle\langle\phi_m|$ with $|\phi_m\rangle \propto \int dx \binom{N}{m} \left(|\vec{q}_1(x)\rangle\right)^{N-m} \otimes \left(e^{i\Delta\vec{q}_2\cdot\hat{x}d} |\vec{q}_2(x)\rangle\right)^{m}$. We see that in this case the photons are in a statistical mixture of all possible ways for passing the slits, and we thus expect a total washout of the interference pattern.

If $N|\Delta\vec{q}_i| \ll \sigma_k$, we can approximate $\Omega_{m\Delta\vec{q}-\vec{k}} \propto e^{-\vec{k}^2/\sigma_k^2}$, so that all integer m will contribute approximately the same to the integration over $d\vec{k_1} d\vec{k_2}$, and $\rho \approx |\phi\rangle\langle\phi|$ with $|\phi\rangle \propto \int dx \sum_{m=1}^{N} \binom{N}{m} \left(|\vec{q}_1(x)\rangle\right)^{N-m} \otimes \left(e^{i\Delta\vec{q}_2\cdot\hat{x}d} |\vec{q}_2(x)\rangle\right)^{m} = \int dx \left(|\vec{q}_1(x)\rangle + e^{i\Delta\vec{q}_2\cdot\hat{x}d} |\vec{q}_2(x)\rangle\right)^{N}$. We see that in this case the photons are approximately all in the same pure state of the simple

(not recoiling) double slit experiment, and we thus still expect measuring an interference pattern. In intermediate cases where $|\Delta\vec{q}_i| < \sigma_k < N|\Delta\vec{q}_i|$, several though not all integers m will contribute to the integration over $d\vec{k}_1 d\vec{k}_2$, and the interference fringes visibility will be between the two extreme limits I discussed - zero and unity.

In order of completing this derivation into a full explanation of saturation we still need to consider many slits, which we did not consider, since the calculation is cumbersome.

Bibliography

[1] M. H. Anderson, J. R. Ensher, M. R. Matthews, C. E. Wieman, and E. A. Cornell, science **269**, 198 (1995).

[2] K. B. Davis, M.-O. Mewes, M. v. Andrews, N. Van Druten, D. Durfee, D. Kurn, and W. Ketterle, Physical review letters **75**, 3969 (1995).

[3] C. Bradley, C. Sackett, J. Tollett, and R. Hulet, Physical Review Letters **75**, 1687 (1995).

[4] B. DeMarco and D. S. Jin, Science **285**, 1703 (1999).

[5] F. Schreck, L. Khaykovich, K. Corwin, G. Ferrari, T. Bourdel, J. Cubizolles, and C. Salomon, Physical Review Letters **87**, 080403 (2001).

[6] A. G. Truscott, K. E. Strecker, W. I. McAlexander, G. B. Partridge, and R. G. Hulet, Science **291**, 2570 (2001).

[7] P. Courteille, R. Freeland, D. Heinzen, F. Van Abeelen, and B. Verhaar, Physical review letters **81**, 69 (1998).

[8] S. Inouye, M. Andrews, J. Stenger, H.-J. Miesner, D. Stamper-Kurn, and W. Ketterle, Nature **392**, 151 (1998).

[9] M. Greiner, O. Mandel, T. Esslinger, T. W. Hänsch, and I. Bloch, Nature **415**, 39 (2002).

[10] C. J. Foot, *Atomic Physics (Oxford Master Series in Atomic, Optical and Laser Physics)*, 1st ed. (Oxford University Press, USA, 2005).

[11] H. J. Metcalf and P. Van der Straten, *Laser cooling and trapping* (Springer, 1999).

[12] J. Dalibard and C. Cohen-Tannoudji, JOSA B **2**, 1707 (1985).

[13] A. Ashkin, Physical review letters **24**, 156 (1970).

[14] S. Chu, J. Bjorkholm, A. Ashkin, and A. Cable, Physical review letters **57**, 314 (1986).

[15] O. Mandel, M. Greiner, A. Widera, T. Rom, T. W. Hänsch, and I. Bloch, Nature **425**, 937 (2003).

[16] S. Hensler, J. Werner, A. Griesmaier, P. Schmidt, A. Görlitz, T. Pfau, S. Giovanazzi, and K. Rzażewski, Applied Physics B **77**, 765 (2003).

[17] T. Lahaye, T. Koch, B. Fröhlich, M. Fattori, J. Metz, A. Griesmaier, S. Giovanazzi, and T. Pfau, Nature **448**, 672 (2007).

[18] L. Corman, J.-L. Ville, R. Saint-Jalm, M. Aidelsburger, T. Bienaimé, S. Nascimbène, J. Dalibard, and J. Beugnon, Physical Review A **96**, 053629 (2017).

[19] R. Saint-Jalm, M. Aidelsburger, J. Ville, L. Corman, Z. Hadzibabic, D. Delande, S. Nascimbene, N. Cherroret, J. Dalibard, and J. Beugnon, arXiv preprint arXiv:1802.04018 (2018).

[20] H. Ritsch, P. Domokos, F. Brennecke, and T. Esslinger, Reviews of Modern Physics **85**, 553 (2013).

[21] D. Nagy, J. Asboth, P. Domokos, and H. Ritsch, EPL (Europhysics Letters) **74**, 254 (2006).

[22] E. Tesio, G. Robb, T. Ackemann, W. Firth, and G.-L. Oppo, Physical Review A **86**, 031801 (2012).

[23] E. Tesio, G. Robb, T. Ackemann, W. Firth, and G.-L. Oppo, Physical review letters **112**, 043901 (2014).

[24] G. Robb, E. Tesio, G.-L. Oppo, W. Firth, T. Ackemann, and R. Bonifacio, Physical review letters **114**, 173903 (2015).

[25] G. Labeyrie, E. Tesio, P. M. Gomes, G.-L. Oppo, W. J. Firth, G. R. Robb, A. S. Arnold, R. Kaiser, and T. Ackemann, Nature Photonics **8**, 321 (2014).

[26] A. Camara, R. Kaiser, G. Labeyrie, W. Firth, G.-L. Oppo, G. Robb, A. Arnold, and T. Ackemann, Physical Review A **92**, 013820 (2015).

[27] Y.-J. Lin, R. L. Compton, K. Jimenez-Garcia, J. V. Porto, and I. B. Spielman, Nature **462**, 628 (2009).

[28] S. Inouye, A. Chikkatur, D. Stamper-Kurn, J. Stenger, D. Pritchard, and W. Ketterle, Science **285**, 571 (1999).

[29] M. Andrews, M. Mewes, N. Van Druten, D. Durfee, *et al.*, Science **273**, 84 (1996).

[30] A. Ashkin, Physical review letters **24**, 156 (1970).

[31] M. Friese, T. Nieminen, N. Heckenberg, and H. Rubinsztein-Dunlop, Nature **394**, 348 (1998).

[32] G. A. Swartzlander Jr, T. J. Peterson, A. B. Artusio-Glimpse, and A. D. Raisanen, Nature Photonics **5**, 48 (2011).

[33] F. Monteiro, S. Ghosh, E. C. van Assendelft, and D. C. Moore, arXiv preprint arXiv:1803.04297 (2018).

[34] Z. Huang, K. Cui, Y. Li, X. Feng, F. Liu, W. Zhang, and Y. Huang, Scientific reports **5**, srep15964 (2015).

[35] E. A. Donley, N. R. Claussen, S. L. Cornish, J. L. Roberts, E. A. Cornell, and C. E. Wieman, Nature **412**, 295 (2001).

[36] E. A. Donley, N. R. Claussen, S. T. Thompson, and C. E. Wieman, Nature **417**, 529 (2002).

[37] C. A. Regal, C. Ticknor, J. L. Bohn, and D. S. Jin, Nature **424**, 47 (2003).

[38] M. Greiner, C. A. Regal, and D. S. Jin, Nature **426**, 537 (2003).

[39] C. Regal and D. Jin, Physical review letters **90**, 230404 (2003).

[40] C. Regal, M. Greiner, and D. S. Jin, Physical review letters **92**, 040403 (2004).

[41] D. Miller, J. Chin, C. Stan, Y. Liu, W. Setiawan, C. Sanner, and W. Ketterle, Physical review letters **99**, 070402 (2007).

[42] J. Siegl, W. Weimer, K. Morgener, K. Hueck, N. Luick, and H. Moritz, in *APS Division of Atomic, Molecular and Optical Physics Meeting Abstracts*, Vol. 1 (2014) p. 1016.

[43] I. Ferrier-Barbut, M. Delehaye, S. Laurent, A. T. Grier, M. Pierce, B. S. Rem, F. Chevy, and C. Salomon, Science **345**, 1035 (2014).

[44] M. Delehaye, S. Laurent, I. Ferrier-Barbut, S. Jin, F. Chevy, and C. Salomon, Physical review letters **115**, 265303 (2015).

[45] D. M. Bauer, M. Lettner, C. Vo, G. Rempe, and S. Dürr, Nature Physics **5**, 339 (2009).

[46] Y. Ding, J. P. D'Incao, and C. H. Greene, Physical Review A **95**, 022709 (2017).

[47] P. Meystre and M. Sargent, *Elements of quantum optics* (Springer Science & Business Media, 2013).

[48] M. Born and E. Wolf, *Principles of optics: electromagnetic theory of propagation, interference and diffraction of light* (Elsevier, 1980).

[49] H. Ritsch, P. Domokos, F. Brennecke, and T. Esslinger, Reviews of Modern Physics **85**, 553 (2013).

[50] K. Tai, A. Hasegawa, and A. Tomita, Physical review letters **56**, 135 (1986).

[51] A. Kim, D. Cattani, D. Anderson, and M. Lisak, Sov. Phys. JETP **81** (2005).

[52] W. Ketterle, D. S. Durfee, and D. M. Stamper-Kurn, (1999), arXiv:cond-mat/9904034 .

[53] S. Stringari, Physical review letters **77**, 2360 (1996).

[54] J. Schoser, A. Batär, R. Löw, V. Schweikhard, A. Grabowski, Y. B. Ovchinnikov, and T. Pfau, Physical Review A **66**, 023410 (2002).

[55] T. Rom, *Bosonische und fermionische Quantengase in dreidimensionalen optischen Gittern*, Ph.D. thesis, lmu (2009).

[56] R. Sahai and L.-Å. Nyman, The Astrophysical Journal Letters **487**, L155 (1997).

[57] J. Goldwin, S. Papp, B. DeMarco, and D. Jin, Physical Review A **65**, 021402 (2002).

[58] C. Klempt, T. Van Zoest, T. Henninger, E. Rasel, W. Ertmer, J. Arlt, *et al.*, Physical Review A **73**, 013410 (2006).

[59] M. Anderson, W. Petrich, J. Ensher, and E. A. Cornell, Physical Review A **50**, R3597 (1994).

[60] T. Walker, D. Sesko, and C. Wieman, Physical Review Letters **64**, 408 (1990).

[61] W. Petrich, M. H. Anderson, J. R. Ensher, and E. A. Cornell, JOSA B **11**, 1332 (1994).

[62] J. Dalibard and C. Cohen-Tannoudji, JOSA B **6**, 2023 (1989).

[63] A. L. Migdall, J. V. Prodan, W. D. Phillips, T. H. Bergeman, and H. J. Metcalf, Physical Review Letters **54**, 2596 (1985).

[64] S. Aubin, S. Myrskog, M. Extavour, L. LeBlanc, D. McKay, A. Stummer, and J. Thywissen, Nature Physics **2**, 384 (2006).

[65] C. Cohen-Tannoudji and D. Guéry-Odelin, World Scientific, Singapore **32**, 36 (2011).

[66] M. Andrews, M.-O. Mewes, N. Van Druten, D. Durfee, D. Kurn, and W. Ketterle, Science **273**, 84 (1996).

[67] N. Matzliah, H. Edri, A. Sinay, R. Ozeri, and N. Davidson, Physical review letters **119**, 163201 (2017).

[68] I. Mazets, The European Physical Journal D- Atomic Molecular and Optical Physics **8**, 371 (2000).

[69] G. Kurizki, S. Giovanazzi, D. O'Dell, and A. I. Artemiev, in *Dynamics and Thermodynamics of Systems with Long-Range Interactions* (Springer, 2002) pp. 369–403.

[70] S. Balik, A. Win, M. Havey, I. Sokolov, and D. Kupriyanov, Physical Review A **87**, 053817 (2013).

[71] L. Corman, J.-L. Ville, R. Saint-Jalm, M. Aidelsburger, T. Bienaimé, S. Nascimbène, J. Dalibard, and J. Beugnon, arXiv preprint arXiv:1706.09698 (2017).

[72] R. Loudon, *The quantum theory of light* (OUP Oxford, 2000).

[73] R. Cline, J. Miller, M. Matthews, and D. Heinzen, Optics letters **19**, 207 (1994).

[74] D. A. Steck, URL http://steck. us/alkalidata **83** (2016).

[75] P. A. Schilpp and H. Jehle, American Journal of Physics **19**, 252 (1951).

[76] M. Jammer, *The philosophy of quantum mechanics: the interpretations of quantum mechanics in historical perspective*, Wiley Interscience publication (Wiley, 1974).

[77] M. Cetina, M. Jag, R. S. Lous, I. Fritsche, J. T. Walraven, R. Grimm, J. Levinsen, M. M. Parish, R. Schmidt, M. Knap, *et al.*, Science **354**, 96 (2016).

[78] I. Bialynicki-Birula and J. Mycielski, Bull. Acad. Polon. Sci. Cl **3**, 461 (1975).

[79] P. Pedri and L. Santos, Physical review letters **95**, 200404 (2005).

[80] J. W. Fleischer, M. Segev, N. K. Efremidis, and D. N. Christodoulides, Nature **422**, 147 (2003).

[81] L. Khaykovich, F. Schreck, G. Ferrari, T. Bourdel, J. Cubizolles, L. Carr, Y. Castin, and C. Salomon, Science **296**, 1290 (2002).

[82] Z. Meir, O. Schwartz, E. Shahmoon, D. Oron, and R. Ozeri, Physical review letters **113**, 193002 (2014).

[83] J. Pellegrino, R. Bourgain, S. Jennewein, Y. R. Sortais, A. Browaeys, S. Jenkins, and J. Ruostekoski, Physical review letters **113**, 133602 (2014).

[84] S. De and I. Spielman, Applied Physics B **114**, 527 (2014).

[85] K. Yosida, Physical Review **106**, 893 (1957).

[86] T. Kasuya, Progress of theoretical physics **16**, 45 (1956).

[87] M. A. Ruderman and C. Kittel, Physical Review **96**, 99 (1954).

[88] W. Ketterle and M. W. Zwierlein, arXiv preprint arXiv:0801.2500 (2008).

[89] U. Levy, K. Yang, N. Matzliah, and Y. Silberberg, Journal of Physics B: Atomic, Molecular and Optical Physics **51**, 035401 (2018).

[90] C. E. Máximo, R. Bachelard, and R. Kaiser, Physical Review A **97**, 043845 (2018).

[91] C. Pearman, C. Adams, S. Cox, P. Griffin, D. Smith, and I. Hughes, Journal of Physics B: Atomic, Molecular and Optical Physics **35**, 5141 (2002).